Dynamical parallax, physical parameters, and evolutionary status of the components of the bright eclipsing binary α Draconis

Pavlovski, K.; Hummel, C. A.; Tkachenko, A.; Dervişoğlu, A.; Kayhan, C.; Zavala, R. T.; Hutter, D. J.; Tycner, C.; Şahin, T.; Audenaert, J.; ...

Download date / Datum preuzimanja: **2024-08-16**

Astronomy & Astrophysics

Dynamical parallax, physical parameters, and evolutionary status of the components of the bright eclipsing binary α Draconis[⋆]

K. Pavlovski[1], C. A. Hummel[2], A. Tkachenko[3], A. Dervişoğlu[4,5], C. Kayhan[4], R. T. Zavala[6], D. J. Hutter[7], C. Tycner[7], T. Şahin[8], J. Audenaert[3], R. Baeyens[3], J. Bodensteiner[3,2], D. M. Bowman[3], S. Gebruers[3], N. E. Jannsen[3], and J. S. G. Momberg[3]

[1] Department of Physics, Faculty of Science, University of Zagreb, 10 000 Zagreb, Croatia
e-mail: pavlovski@phy.hr
[2] European Southern Observatory, Karl-Schwarzschild-Str. 2, 85748 Garching, Germany
[3] Institute of Astronomy, KU Leuven, Celestijnenlaan 200D, 3001 Leuven, Belgium
[4] Department of Astronomy Space Sciences, Science Faculty, Erciyes University, 38030 Melikgazi, Kayseri, Turkey
[5] Astronomy and Space Sciences Observatory and Research Center, Erciyes University, 38281 Talas, Kayseri, Turkey
[6] U.S. Naval Observatory, Flagstaff Station, 10391 W. Naval Obs. Rd., Flagstaff, AZ 86001, USA
[7] Central Michigan University, Department of Physics, Mt. Pleasant, MI 48859, USA
[8] Akdeniz University, Faculty of Science, Department of Space Sciences and Technologies, 07058 Antalya, Turkey

ABSTRACT

Aims. Both components of the bright eclipsing binary α Dra have been resolved using long baseline interferometry and the secondary component has been shown to contribute approximately 15% of the total flux; however, a spectroscopic detection of the companion star has so far been unsuccessful. We aim for a firm spectroscopic detection of the secondary component of α Dra using state-of-the-art spectroscopic analysis methods for very high-quality spectroscopic observations. This will allow the determination of fundamental and atmospheric properties of the components in the system with high precision and accuracy.

Methods. To achieve our goals, we use a combined data set from interferometry with the Navy Precision Optical Interferometer (NPOI), photometry with the TESS space observatory, and high-resolution spectroscopy with the HERMES fibre-fed spectrograph at the La Palma observatory. We use the method of spectral disentangling to search for the contribution of a companion star in the observed composite HERMES spectra, to separate the spectral contributions of both components, and to determine orbital elements of the α Dra system. TESS light curves are analysed in an iterative fashion with spectroscopic inference of stellar atmospheric parameters to determine fundamental stellar properties and their uncertainties. Finally, NPOI interferometric measurements are used for determination of the orbital parameters of the system and angular diameters of both binary components.

Results. We report the first firm spectroscopic detection of the secondary component in α Dra and deliver disentangled spectra of both binary components. The components' masses and radii are inferred with high precision and accuracy, and are $M_A = 3.186 \pm 0.044\,M_\odot$, $R_A = 4.932 \pm 0.036\,R_\odot$, and $M_B = 2.431 \pm 0.019\,M_\odot$, $R_B = 2.326 \pm 0.052\,R_\odot$ for the primary and secondary components, respectively. Combined astrometric and spectroscopic analysis yields the semi-major axis of the system, which is ultimately used to derive the dynamical parallax of $\pi = 11.48 \pm 0.13$ mas, and the distance $d = 87.07 \pm 1.03$ pc to the α Dra system. Evolutionary analysis of both binary components with MESA stellar structure and evolution models suggests the primary is an evolved post-TAMS A-type star, while the companion is a main-sequence A-type star with a convective core mass of $M_{cc} = 0.337 \pm 0.011\,M_\odot$. Positions of both binary components in the Kiel- and HR-diagrams suggest a value of the convective core overshooting parameter f_{ov} well below $0.010\,H_p$, and we infer the age of the system to be 310 ± 25 Myr.

Conclusions. The inferred near-core mixing properties of both components do not support a dependence of the convective core overshooting on the stellar mass. At the same time, the α Dra system provides extra support to hypothesise that the mass discrepancy in eclipsing spectroscopic double-lined binaries is associated with inferior atmospheric modelling of intermediate- and high-mass stars, and less so with the predictive power of stellar structure and evolution models as to the amount of near-core mixing and mass of the convective core.

Key words. stars: fundamental parameters – binaries: spectroscopic – binaries: eclipsing – techniques: interferometric – techniques: spectroscopic – stars: individual: α Dra

1. Introduction

It is a well-known fact that a considerable fraction of stars are born in binary or higher-order multiple systems. In the case of

hot massive OB-stars, binarity or higher multiplicity is found to have a strong effect on their evolution as over 50% of those stars are found in binaries or higher-order multiple systems whose components will interact one or multiple times in the course of their lifetime (e.g., Sana et al. 2012, 2013). Moreover, observational evidence was recently presented that the binary fraction among massive stars is independent of their environment. As such, Almeida et al. (2017) demonstrate that O-type stars in

---

the 30 Dor region of the Large Magellanic Cloud (LMC) show the observed binary fraction of approximately 55–60% that is similar to the existing Galactic samples of massive stars. Furthermore, Bodensteiner et al. (2021) and Banyard et al. (2022) report similar binary fraction of 50–55% among SMC and Galactic B-type stars, respectively. At the same time, Luo et al. (2021) report a somewhat lower binary fraction of approximately 40% among Galactic OB-stars from LAMOST low-resolution multi-epoch spectroscopy. Finally, Cohen et al. (2020) report the binary fraction among solar-type stars to be about 42% suggesting that binarity is a key player in the evolution and fate of stars, independently of their initial mass.

Given the large binary fraction among solar-type (Duchêne & Kraus 2013), and more massive stars (Sana et al. 2014), binarity can become a serious obstacle for interpretation of astrophysical results when it is not properly accounted for. For example, detailed chemical composition analysis of stars may reveal complex and spurious abundance patterns when a faint and spectroscopically undetected companion is not accounted for in the spectroscopic analysis (Schöller et al. 2010). Furthermore, observationally undetected stellar pairs can lead to the appearance of multiple parallel main sequences in the Hertzsprung-Russell (HR) diagrams from photometric surveys (Kroupa et al. 1993; Elson et al. 1998). Moreover, ignorance of the orbital motion of the two stars in a binary system also leads to a large bias in the astrometric measurement of the stellar parallax (Makarov & Kaplan 2005; Frankowski et al. 2007; Kervella et al. 2019). Finally, classification of a star as an X-ray source or a flaring object can be erroneous when a possible companion star remains undetected (Schröder & Schmitt 2007; Stelzer et al. 2011).

On the other hand, when the subject of targeted research, spectroscopic double-lined or eclipsing binaries, if spatially resolved, become a principal source of the fundamental stellar quantities such as masses and radii of stars. With the advent of observational instruments and techniques, such as high-precision and high-resolution spectroscopy, high angular resolution interferometry, and micro-magnitude precision and high duty cycle space-based photometry, stellar masses and radii are more routinely measured than ever before, with accuracy better than 3% (Torres et al. 2010; Serenelli et al. 2021). High-precision and high-accuracy measurements of fundamental and atmospheric properties of stars are a challenge to the theory of stellar structure and evolution (SSE), but also offer a powerful tool for the improvement of the SSE theory. Over the last two decades spectroscopic double-lined eclipsing binaries have been extensively exploited to study the effects of the stabilisation of thermal convection by magnetic fields and of atomic diffusion in low-mass stars (e.g., Feiden & Chaboyer 2012, 2013, 2014; Torres et al. 2014; Higl & Weiss 2017), to probe the levels of near-core mixing (typically in the form of convective core overshooting) in intermediate- and high-mass stars (e.g., Pols et al. 1997; Guinan et al. 2000; Claret & Torres 2016, 2017, 2018, 2019; Martinet et al. 2021), to investigate chemical element transport from accurate measurements of surface abundances in massive stars (Pavlovski et al. 2018), and to measure convective core masses in intermediate- and high-mass BA-type stars (e.g., Johnston et al. 2019a; Tkachenko et al. 2020).

Today, binary stars are often found to be synergistic with intrinsically variable stars, where the variability is typically caused by stellar pulsations, rotational modulation of surface inhomogeneities, and activity of cool companion stars. Hence, combining complementary research approaches (e.g., asteroseismology and binarity) and/or observational techniques (e.g.,

spectroscopy, astrometry, and photometry) allows us to attack the problem of uncertainties in SSE models from various angles, where SB2 EBs play a crucial role.

In this work we study α Dra (also known as Thuban), a bright ($V = 3.7$ mag) binary system that was first reported as such by Harper (1907). Following the recent detection of eclipses in the photometric data recorded with the Transiting Exoplanet Survey Satellite (TESS, Ricker et al. 2014, 2015) by Bedding et al. (2019) and the possible detection of a faint companion star in high-resolution spectra by Hey et al. (2022), we acquired a new set of high-resolution optical spectra, complementing already-existing high angular resolution interferometric data, to enable a high-precision study of the system. In Sect. 2 we provide a short overview of the previous studies of the α Dra system. Results of the analysis of Mark III and NPOI interferometric, HERMES high-resolution optical spectroscopic, and TESS space-based photometric data are presented in Sects. 3–5, respectively. We assess the evolutionary status of both binary components in Sect. 6, while the dynamical parallax measurement is provided in Sect. 7 along with discussion on all the distance estimates to the system available to date. We present a general discussion of the obtained results in Sect. 8, and close the paper with conclusions and an outline of future work in Sect. 9.

2. An overview of α Dra

Since the first determination of the orbital parameters by Harper (1907), α Dra (11 Dra, HD 123299) was frequently observed spectroscopically as a SB1 system. A high degree of consistency is observed for orbital solutions reported by different research groups, yet some of the reported differences are statistically significant as they are larger than the quoted uncertainties. For example, Elst & Nelles (1983) report the radial velocity (RV) semi-amplitude of $K = 49.8 \pm 0.3$ km s^{-1} for the visible component, while more recent studies by Kallinger et al. (2004) and Bischoff et al. (2017) find $K = 48.488 \pm 0.080$ km s^{-1} and $K = 47.48 \pm 0.21$ km s^{-1}, respectively. Since α Dra has not been recognised as a SB2 system yet, all previous inferences of RV semi-amplitude are likely to be affected by the broad spectral features of an as yet undetected companion star. No appreciable changes in the longitude of periastron ω indicative of an apsidal motion are reported in the literature; the system is found to reside in a highly eccentric orbit, $e = 0.426 \pm 0.004$ (Bischoff et al. 2017). The star was also first resolved with the Navy Precision Optical Interferometer (NPOI), and an estimate of the brightness difference of $\Delta m = 1.83 \pm 0.07$ mag at $\lambda 7000$ Å was derived by Hutter et al. (2016).

Adelman et al. (2001) performed a detailed abundance analysis of α Dra based on DAO spectrograms, and classified the system as a λ Bootis star owing to the detected metal deficiencies. More recently, however, α Dra has been withdrawn from a list of λ Boo candidate stars by Murphy et al. (2015). A historical disagreement as to the true value of the projected rotational velocity of the star was finally resolved thanks to the advent of electronic detectors and the high spectral resolution of the instruments. Gray (2014) measured $v \sin i$ of 26.2 km s^{-1} from a high-resolution and high signal-to-noise spectrum using the Fourier transform technique. The measurement is in good agreement with the findings by Royer et al. (2002) and Shorlin et al. (2002), who report $v \sin i$ of 25 ± 2 km s^{-1} and 28 ± 2 km s^{-1}, respectively.

A dedicated spectroscopic observational campaign was organised by Kallinger et al. (2004) to search for possible intrinsic variability in the star through a study of line profile variations.

Table 1. NPOI calibrators.

HD	Sp. type	V [mag]	$V - K$ [mag]	$E(B - V)$ [mag]	θ_{V-K} [mas]	V^2_{min}
FK5 423	A2V	3.34	0.26	−0.06	0.86	0.88
FK5 447	A0V	2.44	0.01	0.02	1.11	0.81
FK5 456	A3Vv	3.31	0.21	0.00	0.84	0.90
FK5 472	B6IIIp	3.87	0.05	0.02	0.59	0.89
HR 5062	A5V	4.01	0.87	0.01	0.67	0.95
FK5 509	B3V	1.86	−0.41	0.01	1.11	0.81
HR 5329	A8IV	4.54	0.44	−0.05	0.56	0.79
FK5 622	O9.5V	2.60	−0.08	0.29	0.00	1.00
FK5 668	A0V	3.75	0.13	0.06	0.65	0.93
FK5 677	B5Ib	3.97	−0.03	0.12	0.50	0.97
FK5 913	A1Vn	4.36	0.10	0.01	0.48	0.99

Notes. V^2_{min} is minimum (squared) visibility on the longest baselines used.

Their data set consists of 140 echelle spectra secured during ten nights in January 2003 at the Observatoire de Haute-Provence (OHP) and 1150 time-resolved high-resolution spectra acquired during 45 nights in 2003–2004 at the Türinger Landessternwarte Tautenburg. Kallinger et al. (2004) report the detection of periodic RV variations at a frequency of 26.5 d^{-1} and with variable orbital phase-dependent amplitude. The authors conclude that the observed periodic RV variability is caused by the interaction between tides in the system and a pulsation driving mechanism intrinsic to the star.

In the HR diagram α Dra is positioned between the instability strips of δ Sct and slowly pulsating B-type (SPB) stars. This triggered a speculation that α Dra might belong to a loosely defined class of Maia variable stars, named after the B8-type prototype Maia star in the Pleiades (Struve 1955). Although the variability of Maia itself was disproved by Struve et al. (1957), the speculation about a new class of intrinsically variable stars was reintroduced by Mowlavi et al. (2013) who reported the detection of 36 stars in NGC 3766 that were found to reside in between the δ Sct and SPB instability strips and whose variability was attributed to stellar pulsations. Moreover, a recent study of the seven brightest B-type stars in the Pleiades by White et al. (2017) concludes that six of these objects are SPB stars, while Maia itself exhibits photometric variability with a period of about ten days that is caused by rotational modulation of a large chemical spot. Absence of rapid line profile variations is also reported by Monier (2021) based on the analysis of FEROS and NARVAL high-resolution spectra. Finally, Balona et al. (2015) presented a study of a large sample of B-type stars in the *Kepler* field and classified all stars with high-frequency variability that are cooler than 20 000 K as Maia variables. It is worth noting that the study by Balona et al. (2015) does not provide a solid proof of the existence of Maia variables, instead it once again reintroduced the speculation about an unknown class of variables among B-type stars.

Bedding et al. (2019) investigated two sectors of TESS space-based photometric data of α Dra and report the detection of primary and secondary eclipses separated by about 38.5 d. The authors also inspect the TESS light curve for signatures of intrinsic variability and find no evidence for it at the level of ten parts per million. This result is in contradiction with the findings by Kallinger et al. (2004) who reported spectroscopic variability on timescales of 1 hr. More recently, Hey et al. (2022) performed a study of α Dra based on the combined TESS photometry and newly obtained high-resolution SONG spec-

troscopy. The authors find a hint of a faint secondary component in the strongest absorption lines in the archival SOPHIE spectra of the system, yet spectral disentangling proved difficult owing to the low flux contribution from a companion star and its rapid rotation ($v \sin i \sim 200 \, km \, s^{-1}$). Based on the results of a combined light curve and RV curve analysis, and using MIST isochrones, Hey et al. (2022) constrain T_{eff} and the mass of the primary to be 9975 ± 125 K and $3.7 \pm 0.1 \, M_\odot$, respectively. From the measured inclination and mass function of the system, the authors report a minimum mass of the secondary component to be $2.5 \pm 0.1 \, M_\odot$. In addition, their chemical composition analysis of the high signal-to-noise ratio co-added SOPHIE spectrum reveals a complex abundance pattern for the primary component, and the authors confirm the claim of Bedding et al. (2019) on the absence of intrinsic variability in the TESS photometric data.

3. High angular resolution interferometry

3.1. Observations, data reduction, and calibration

α Dra was observed with the Mark III interferometer[1] (Shao et al. 1988) and with the NPOI (Armstrong et al. 1998). The observation log is given in Table A.1 with information about the baseline lengths and calibrators used. The Mark III data, recorded in narrow-band channels centred at 500 nm, 550 nm, and 800 nm, were reduced and the visibilities calibrated as described by Mozurkewich et al. (2003). Even though baselines of different lengths could be configured, the Mark III operated only a single baseline during each night, so that no closure phases were obtained.

The reduction of early NPOI data using a three-way combiner was described by Hummel et al. (1998), and for the six-way combiner (data from 2002) by Hummel et al. (2003). The data consist of visibilities and closure phases.

The calibrators were taken from a list of single stars maintained at NPOI with diameters estimated from V and $(V - K)$ using the surface brightness relation published by Mozurkewich et al. (2003) and van Belle et al. (2009). Values for $E(B - V)$ were derived by comparing the observed colours to theoretical colours as a function of spectral type by Schmidt-Kaler in Aller et al. (1982). Values for the extinction derived from $E(B - V)$ were compared to estimates based on maps by Drimmel et al. (2003), and used to correct V if they agreed within 0.5 magnitudes. Even though the surface brightness relationship based on $(V - K)$ colours is to first order independent of reddening, we included this small correction. The minimum (squared) visibility amplitudes corresponding to the diameter estimates are given in Table 1 for any NPOI observation performed, and show that the calibrator stars are mostly unresolved or only weakly resolved.

3.2. Orbital analysis

Modelling of the (squared) visibility amplitudes (Fig. 1) and closure phases was performed with OYSTER[2]. Each night's data were fit using a binary model parametrised with the angular diameters of the two stars, their magnitude difference, and their relative position. The stellar parameters were not free to vary in this step, but were constrained with the orbital elements replacing the relative positions in a fit directly to all visibility data. To

---

[1] Decommissioned in 1992.
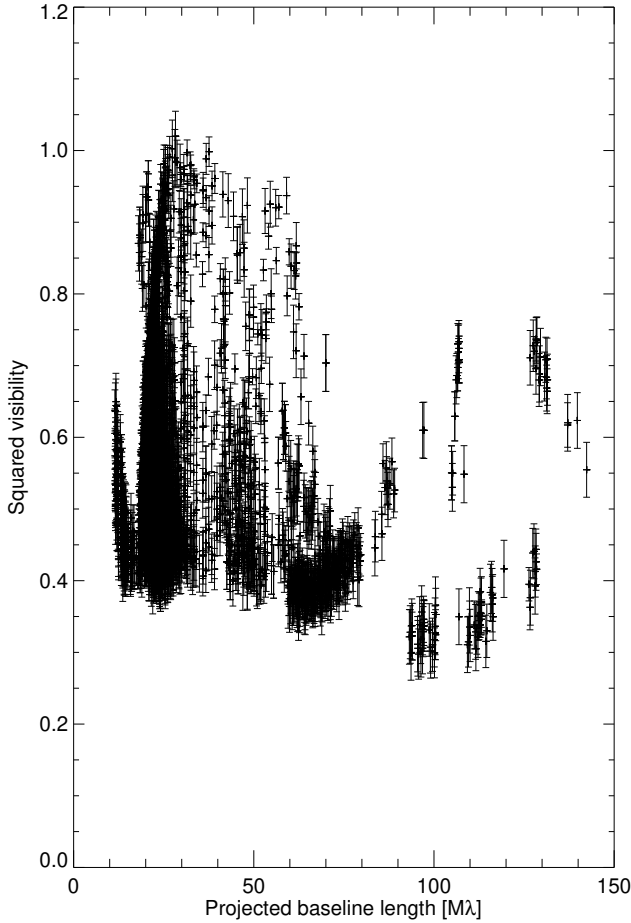[2] https://www.eso.org/~chummel/oyster/oyster.html

Fig. 1. Measured (squared) visibility amplitudes plotted against *uv* radius. For clarity, only data with errors less than 4% are shown. The decreasing upper envelope of the visibility amplitudes indicates that the primary component is well resolved, while the weaker trend of the lower envelope indicates a smaller diameter for the secondary. The strong amplitude variation in between is due to the interference pattern caused by the binarity of the source structure.

better constrain the orbital period, we added radial velocity measurements from historical sources (Pearce 1957; Elst & Nelles 1983; Adelman et al. 2001; Bischoff et al. 2017). The smaller diameter of the secondary, which is not well constrained in this fit, was estimated in a second fit by adopting the effective temperatures and surface gravities derived in this work and the diameter of the primary. The astrometric results are summarised in Tables 2 and A.2, and the apparent orbit of resolved binary system of α Dra is shown in Fig. 2. The astrometric error ellipses were derived from fitting the 4σ contour of the minimum of the χ^2 surface around the secondary's position, normalised to unity.

4. High-resolution spectroscopy

4.1. New HERMES high-resolution spectroscopy

New high-resolution echelle spectra were obtained from 10 February to 1 April 2021 at the 1.2 m Mercator telescope at the Observatorio del Roque de los Muchachos, La Palma, Canary Islands, Spain. The spectra were secured with the HERMES fibrefed high-resolution ($R = 85\,000$) spectrograph (Raskin et al. 2011). The HERMES spectra cover the entire optical spectral range from 3770 to 9000 Å in 55 spectral orders. Depending on zenith distance, exposure times ranged between 40 s and 120 s

Table 2. Orbital elements and component parameters for α Dra.

Parameter	Unit	Value ± Error
Period P	[d]	51.417350 ± 0.00034
Periastron epoch T_{pp}	[JD]	2453498.8 ± 0.1
Eccentricity e		0.43 ± 0.01
Periastron angle ω	[deg]	22.4 ± 0.5
Ascending node Ω	[deg]	252.6 ± 0.4
Inclination i	[deg]	85.4 ± 0.5
Semi-major axis a''	[mas]	5.52 ± 0.06
Magnitude difference ΔR	[mag]	1.79 ± 0.02
Primary's diameter D_A	[mas]	0.62 ± 0.05
Secondary's diameter D_B	[mas]	0.28 ± 0.05

Notes. Ascending node is for epoch J2000.0, and the periastron angle is that of the primary.
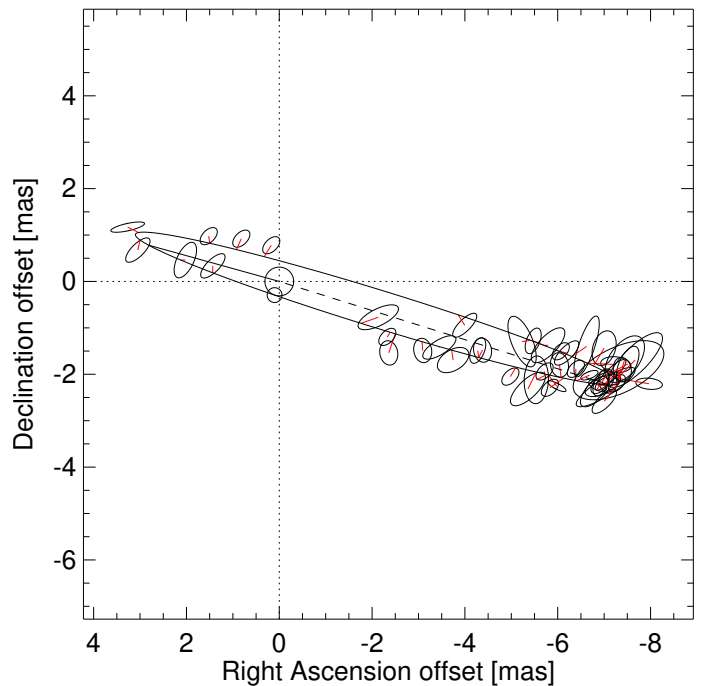

Fig. 2. Apparent orbit of α Draconis. The solid straight line indicates the periastron, and the dashed line the ascending node. The two small circles near the origin indicate the interferometric sizes of the primary and secondary components at inferior conjunction.

for a typical signal-to-noise ratio (S/N) of over 200. In total 50 spectra were collected, of which 4 were discarded for an insufficient S/N.

The reduction of the raw observations was performed with a dedicated HERMES data reduction pipeline. The individual reduction steps include background and bias subtraction, flat fielding, wavelength calibration using a ThArNe lamp, and echelle order merging. Reduced spectra are resampled in constant velocity bins preserving the size of the detector pixels. Continuum normalisation is done manually by fitting a spline function to a carefully selected set of pseudo-continuum points.

4.2. Spectroscopic detection of the secondary component

As discussed in detail in Sect. 2, α Dra has so far been classified as a SB1 system, and only recently did Hey et al. (2022) find a
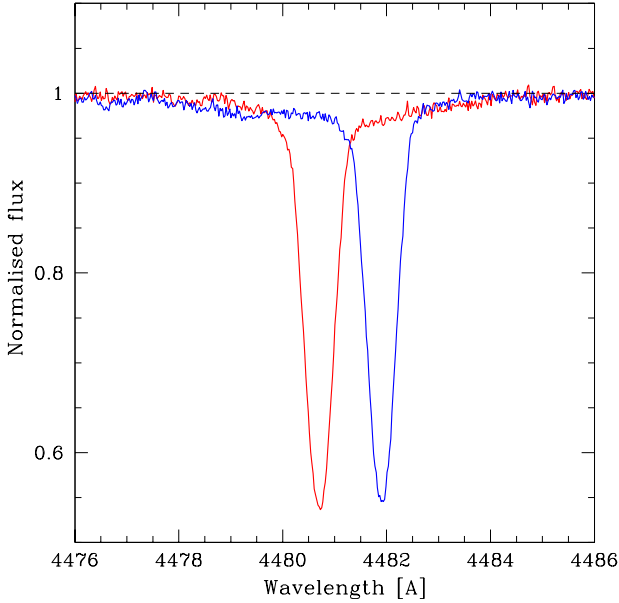
Fig. 3. Two observed composite HERMES spectra taken at quadrature in the region of the Mg II 4481 Å spectral line. A broad and shallow spectral feature of the secondary component is clearly seen at about 1% of the continuum. A fiducial pseudo-continuum is indicated with the dashed line for reference. The spectra were obtained on BJD 2 459 286.64516 (red line) and BJD 2 459 305.62250 (blue line), and correspond to the phases of the orbital cycle 0.486 and 0.856, respectively.

hint of a companion star in a high S/N archival SOPHIE spectrum. According to the interferometric measurements, the magnitude difference between the two stars is $\Delta m = 1.81 \pm 0.02$ mag, such that a companion star contributes approximately 15% to the total light. Therefore, we suspect that the lack of detection of signatures of the secondary component in the observed composite spectra of the system so far is probably associated with its rapid rotation, as also hypothesised by Hey et al. (2022). Therefore, our HERMES spectroscopic campaign was specifically tuned to a detection of broad and shallow lines of a companion star, hence the requirement for high S/N and full orbital phase coverage. A visual inspection of the normalised HERMES spectra confirms the suspicion: a broad and shallow depression in the continuum is clearly visible around prominent metal lines in the composite spectra of the system. This is illustrated in Fig. 3 where two spectra taken at quadrature are shown in the region of the Mg II 4481 Å spectral line.

Spectral disentangling is an efficient method for extracting the spectra of the individual components, while simultaneously optimising the orbital elements of a binary (or higher-order multiple) system (Simon & Sturm 1994). A time series of the observed spectra, preferably of high resolution and uniformly distributed with the orbital phase, is required for the task. The method has proved to be very efficient in revealing even very faint companions, contributing as little as 1–2% to the total light of the system (e.g., Mayer et al. 2013; Torres et al. 2014; Kolbas et al. 2015; Themeßl et al. 2018).

We employed spectral disentangling in the Fourier space as proposed by Hadrava (1995) and implemented in the FDBINARY software package (Ilijic et al. 2004). A complete procedure was worked out in Hensberge et al. (2000), and elaborated and refined in detail in Pavlovski et al. (2018). We applied the method to our data set of HERMES high-resolution spectra, start-

ing with prominent metal lines such as those of the Mg II 4481 Å doublet. This procedure leads us to unambiguously detect the spectral contribution of the secondary component; Fig. 4 shows a portion of the disentangled spectra of both binary components in the regions of the Mg II 4481 Å doublet (left panel), the spectral line blends of Fe II 4549.5 and Ti II 4549.7 Å (middle panel) and Fe II 5316.6 and Fe II 5316.8 Å (right panel). Spectral lines of the secondary component are shallow, with depths at the level of 1% of the continuum, owing to its high rotational velocity. We note that the detection of such a faint contribution is only possible when several conditions are simultaneously met: (i) a high resolving power of the instrument, (ii) a high S/N of the observed composite spectra, and (iii) optimally extracted and normalised spectra. The last aspect is particularly important for the successful reconstruction of the individual spectra of (faint) binary components. Furthermore, a proper selection of spectral segments for Fourier-based disentangling is essential; particular attention should be paid to placing the edges of selected spectral intervals in the (pseudo-)continuum regions that are free of spectral lines. Violation of this condition leads to large-amplitude continuum undulations in the disentangled spectra, which affect the line depths.

Interferometric and photometric analyses of the α Dra system presented in Sects. 3 and 5, respectively, unambiguously identify the star as a detached binary system. Both components are found to be well-bounded within their Roche lobes, and there is barely any light variation detected outside the partial eclipses in the TESS light curve. In the cases when changes in the light ratio between the two components are absent and/or eclipse spectra are missing, an ambiguity occurs in the spectral disentangling. Since the zeroth-order term in the Fourier expansion is indeterminable, the line depths in the disentangled spectra are not uniquely determined (Pavlovski & Hensberge 2005). In this case the best approach is to perform spectral disentangling in the 'pure separation' mode (Pavlovski & Hensberge 2010), of which the net result is the separated spectra of the individual components that are diluted according to the light ratio of the two stars. Two options are available for further analysis of the separated spectra: (i) they are re-normalised to their individual continua using the light ratio inferred from the light curve analysis or (ii) the light ratio can be used as a free parameter in spectroscopic analysis along with atmospheric parameters of the star.

An important aspect of spectral disentangling is a S/N gain in the resulting disentangled spectra. Spectral disentangling is acting as co-addition of the observed spectra, so the expected gain is proportional to $\sqrt{N}$, where N is the number of observed composite spectra. The gain in S/N is distributed to both disentangled spectra proportional to the fractional light contribution of a component to the total light of the system. For α Dra we obtain S/N of ~1470 and ~260 for the primary and secondary component, respectively.

The final separation of the component spectra of α Dra from our newly obtained set of HERMES spectra was performed with the orbital parameters determined in Sect. 4.3. The disentangled spectra cover a wavelength range from 4000 Å to 5650 Å, including the prominent Hβ, Hγ, and Hδ Balmer lines. These spectra are used for our detailed spectrum analysis in Sect. 4.4.

4.3. Spectroscopic orbit from spectral disentangling

In the spectral disentangling method, orbital elements are optimised based on a time series of the observed spectra in a self-consistent manner, along with the reconstruction of the
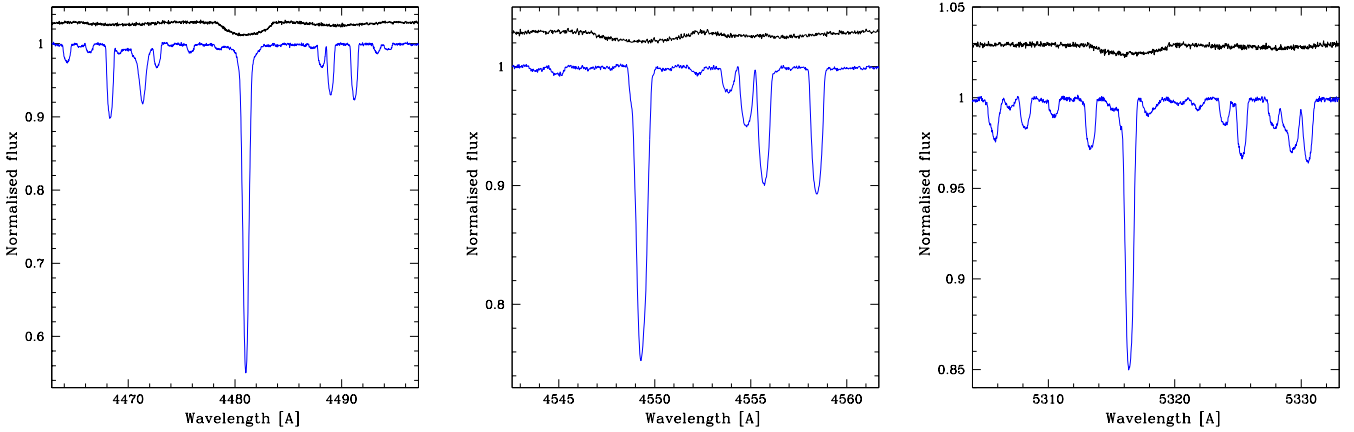
Fig. 4. Small portions of the disentangled spectra of the primary (blue line) and secondary (black line) components of the α Dra system. From left to right: Mg II 4481 Å doublet, the Fe II 4549.5 and Ti II 4549.7 Å spectral blend, and the Fe II 5316.6 and Fe II 5316.8 Å spectral blend. The secondary's disentangled spectrum is arbitrarily shifted for clarity.
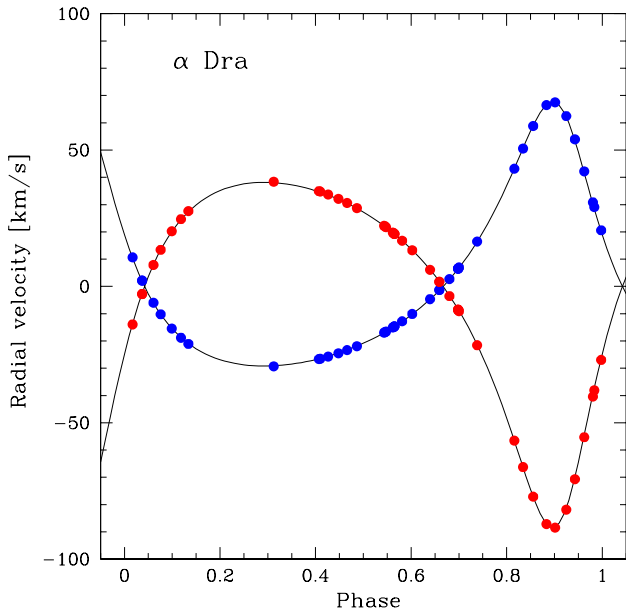

Fig. 5. Radial velocities computed from the final orbital solution. The blue and red dots refer to the primary and secondary component, respectively. The obtained spectroscopic orbital solution is indicated with the black solid line.

individual component spectra (Simon & Sturm 1994; Hadrava 1995). In this way the determination of RVs from the individual exposures is not needed. The spectra of both components of the α Dra system are dominated by strong and broad hydrogen lines, which are not the best diagnostic lines for determining the orbital parameters of the system, irrespective of whether the parameters are inferred from one of the RV determination methods or from the method of spectral disentangling. There are two main reasons why Balmer lines in A-type stars are not suitable for the task. First, owing to their strengths and widths, hydrogen lines are typically covered by two echelle orders which make them subject to systematic uncertainties in the order merging and normalisation to the local continuum. Second, hydrogen lines in the individual component spectra are rarely sufficiently well separated in velocity space, which leads to a more uncertain orbital solution. In the case of the α Dra system, both of the above-mentioned obstacles are present, hence we do not use the

Balmer lines in the determination of the orbital parameters of the system.

To ensure that a sufficient number of metal lines are considered for the determination of orbital parameters of the system, and to make the best use of the high quality of the extracted and normalised HERMES spectra, we opted for the spectral disentangling in large spectral segments of about 350 Å, from 4400 Å to 4750 Å, and about 500 Å, from 5000 Å to 5500 Å. Our final solution is given in Table 3; RVs computed from the finally adopted spectroscopic orbital parameters are shown in Fig. 5 and are representative of the obtained orbital phase coverage.

4.4. Atmospheric parameters

For the analysis of the disentangled spectra, we employ the software package Grid Search in Stellar Parameters (GSSP; Tkachenko 2015). The method is based on the comparison of a grid of synthetic spectra to the observed spectrum of the star and the quality of the fit is judged on the χ^2 merit function. GSSP allows for the simultaneous optimisation of five atmospheric and line-broadening parameters, namely effective temperature $T_{\rm eff}$, surface gravity $\log g$, metallicity [M/H], microturbulent velocity ξ, and projected rotational velocity $v \sin i$ of the star. Optionally, the effect of light dilution on the disentangled spectrum can also be taken into account by either assuming that the light dilution factor is wavelength independent (as implemented in the GSSP_SINGLE module; Tkachenko 2015, their Eq. (1)), or by replacing it with the ratio of the radii of the two stars, where the wavelength dependence of the light dilution effect is introduced via the continuum ratio of the binary components (as implemented in the GSSP_BINARY module; Tkachenko 2015, their Eq. (4)). The latter approach is justified in the cases where binary components have significantly different effective temperatures, otherwise the assumption of the wavelength-independent light dilution factor is robust. Given that our spectroscopic and photometric analyses of the α Dra system both show that the binary components have nearly identical effective temperatures, we limit ourselves to the analysis with the GSSP_SINGLE module where the light dilution factor is assumed to be independent of wavelength.

The GSSP package employs a grid of atmosphere models pre-computed with the LLMODELS program of Shulyak et al. (2004) (for the summary of the grid properties, see the Table 1 of Tkachenko 2015), while theoretical spectra are computed 'on the
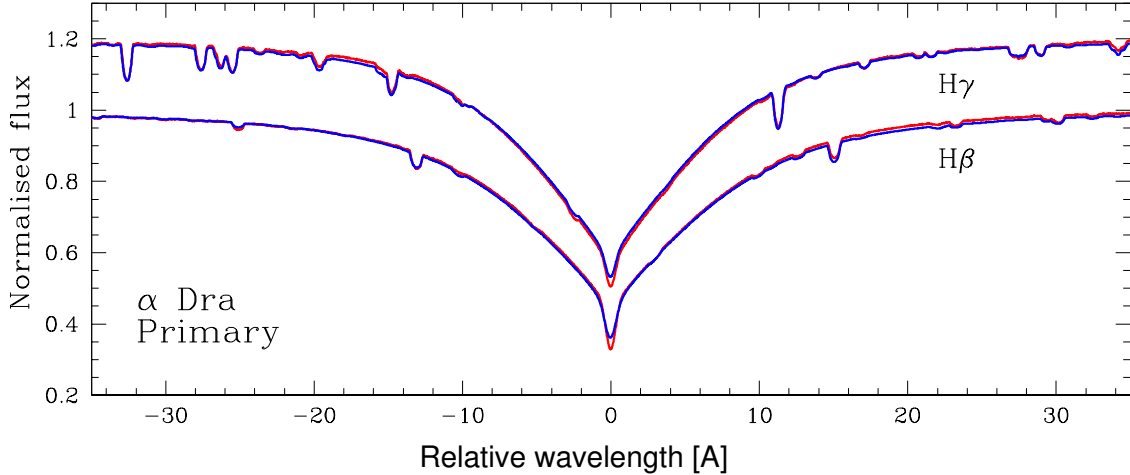
Fig. 6. Comparison between the best fit synthetic (blue lines) and the observed disentangled (red lines) spectra of the primary component in the regions of Hγ (upper profile) and Hβ (lower profile) Balmer lines. Both profiles are shown relative to their central wavelengths; the corresponding best fit atmospheric parameters are listed in Table 4 (Run 2b). The spectra centred on Hγ are arbitrarily shifted for better visibility.

fly' with the SYNTHV (Tsymbal 1996) spectrum synthesis code. The χ^2 merit function is computed for each pair of the observed-theoretical spectra in the grid, and 1σ uncertainties are computed from χ^2 statistics by projecting all χ^2 values on the parameter in question. In this way we take into account possible correlations between the free parameters in our model.

The spectroscopic analysis is performed iteratively with the analysis of the TESS light curve (see Sect. 5). We start with the analysis of the disentangled spectrum of the primary component only, and optimise the following six parameters: T_{eff}, log g, [M/H], ξ, $v \sin i$, and the light dilution factor. The results of this analysis are summarised in Table 4 (column 'Run 1') and suggest the primary component is a somewhat evolved A-type star with a close-to-solar metallicity. A light curve solution can then be obtained with the T_{eff} value of the primary component fixed to 10 190 K, in turn delivering photometric values of the surface gravity and light dilution factor for both binary components.

In the next step of the spectroscopic analysis, we analyse the disentangled spectra of both binary components by fixing the log g values for both stars to their photometric values while keeping all other parameters free. It is important to note that we exclude broad Balmer lines from the analysis of the disentangled spectrum of the faint secondary component as they are found to be non-negligibly distorted in the disentangling process. This issue is not present in the disentangled spectrum of the primary component thanks to its dominance in the observed composite spectra of the α Dra system. The results of the spectroscopic analysis are reported in Table 4 (column 'Run 2a'). As can be seen, the parameters of the primary component barely change compared to the previous iteration (columns Run 1 vs. Run 2a). Furthermore, we find a good agreement between the spectroscopic and photometric T_{eff} values for the secondary component.

On the other hand, we obtain a slightly larger value for the light dilution factor of the secondary compared to its photometric value, and the secondary appears to be slightly metal deficient compared to the primary component. Because we fit a region of the secondary's spectrum free of hydrogen lines, there is a significant degeneracy between the light dilution factor and the metallicity parameter of the star. Therefore, in the final iteration of the spectroscopic analysis, we decided to fix the light factors of both binary components to the values inferred from the light curve solution in addition to the previously fixed values of log g. Our finally accepted spectroscopic parameters of both

binary components are listed in Table 4 (column 'Run 2b'), and suggest that, within the quoted 1σ uncertainties, the two stars have equal effective temperatures and metallicities. On the other hand, the primary component is found to be more evolved and to have substantially lower projected rotational velocity than its companion star. The quality of the fit of the disentangled spectra corresponding to the finally accepted atmospheric parameters is illustrated in Figs. 6 and 7.

Adopting the light ratio determined in the TESS light curve analysis ($\ell_B/\ell_A = 0.212 \pm 0.014$) in the final iteration of the optimal fit of disentangled spectra needs justification since the TESS passband covers the red and the near-IR part of the spectrum, from about $\lambda\lambda$ 6000–10 000 Å, with an effective wavelength of about $\lambda = 7865$ Å (the TESS passband is centred at the standard Cousins I passband, as given in Ricker et al. 2014). The optimal fitting of disentangled spectra are performed on a 500 Å spectral segment centred at about 5250 Å, and on a 350 Å spectral segment centred at about 4570 Å. We performed the calculation of the light ratio as a function of the wavelength using the spectral energy distribution for both stars. It was found that changes from the spectral region centred at 5200 Å to the spectral range covered by the TESS passband is within the assigned uncertainties, and barely about 1%. Therefore, we conclude that our assumption on the constant light ratio for the entire spectral range analysed is justified.

5. TESS space photometry

5.1. Observations

α Dra (TIC 165991532) was observed by the Transiting Exoplanet Survey Satellite (TESS, Ricker et al. 2014, 2015) at five different sectors with a 2 min cadence. At the time of this study, Sectors 14, 15, 16, 21, and 22 of the TESS data were available for α Dra. To extract the light curves we used the target pixel files (TPFs) from the Mikulski Archive for Space Telescopes (MAST) database. Because of the brightness of α Dra ($V = 3.68$ mag), the reduction methods utilised to construct the simple aperture photometry (SAP) or Pre-Search Data Conditioning Simple Aperture Photometry light curves from MAST (PDCSAP, Smith et al. 2012) proved to be less than ideal and led to anomalies in the extracted light curves. Instead, we employ
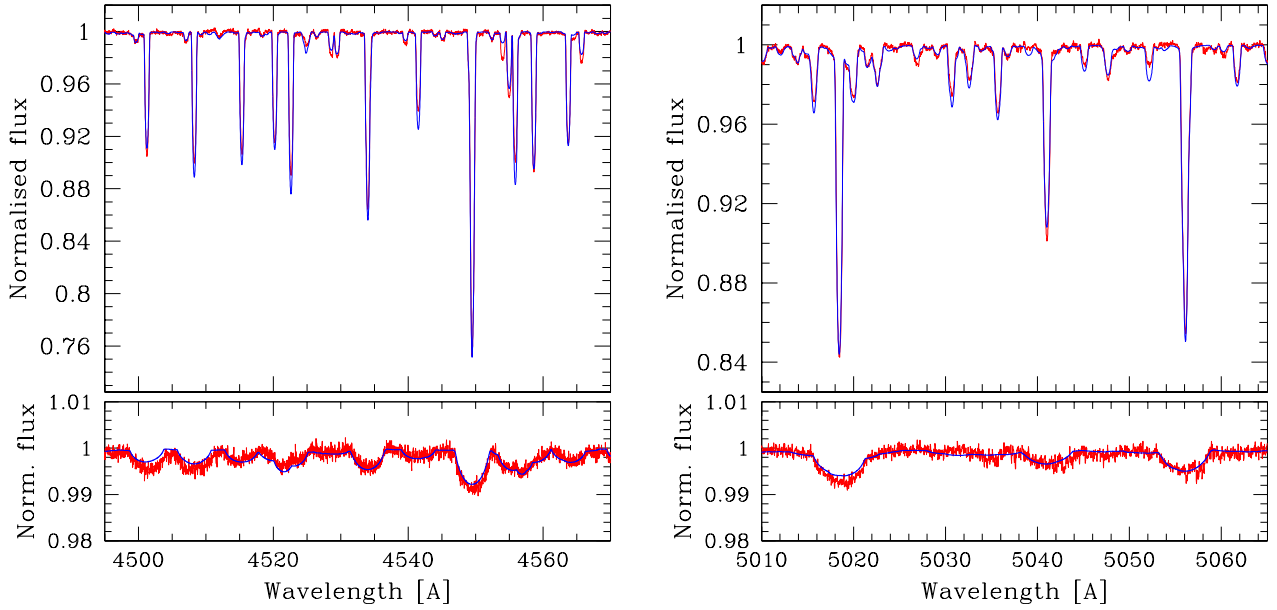
Fig. 7. Quality of the fit (blue) to the disentangled spectra (red) of the primary (*top panels*) and secondary (*bottom panels*) in two metal line regions: $\lambda\lambda$ 4495–4570 Å (*left column*) and $\lambda\lambda$ 5010–5065 Å (*right column*). We note the difference in the *Y*-axis between the top and bottom panels owing to the small relative light contribution and rapid rotation of the secondary component.
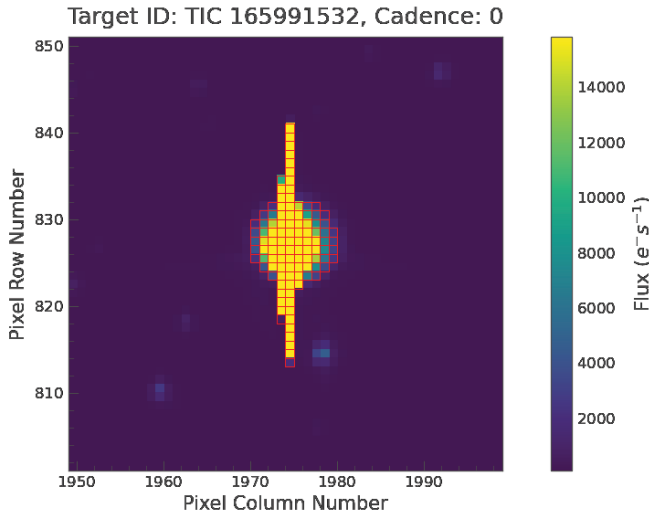

Fig. 8. Target pixel file of α Dra in Sector 15. Our custom mask (red) and bright pixels of the target (yellow) are easily seen. The aperture to obtain the light curve that is represented with our custom mask (red) covers all the bright pixels of the target. To obtain the light curve, all pixels outside the mask that are background and nearby star light contamination are subtracted.

the LIGHTKURVE software package (Cardoso 2018) to produce a target custom mask, and to estimate and subtract the background in each TESS sector. For that purpose, we utilise the median flux value computed across the TPF and the standard deviation estimated from the median absolute deviation (MAD) of the data set. The MAD and the standard deviation are related through a scale factor k that is taken to be 1.4826, assuming normally distributed data. All pixels whose flux values are found to exceed a certain threshold (computed as a number of standard deviations from the median flux value) are considered to belong to the target custom aperture, while pixels with the flux values below the threshold are considered to be background. Here we find through a set of experiments the threshold value of nearly 30% of the maximum

flux amplitude pixel to be the optimal one, and consider all pixels with fluxes below (above) to be background (target custom aperture). The background flux is estimated and subtracted per pixel over time, which allows us to minimise the noise contribution and to remove light contamination from the nearby (background) stars. Figure 8 shows an example of the TESS TPF and our custom aperture selection (red), used to obtain a light curve of α Dra from Sector 15 of the TESS data. The same method is used to extract light curves from other sectors of the available TESS data.

In total, from the above-mentioned five TESS Sectors, we obtained 91173 photometric measurements that cover three primary and two secondary minima and out-of-eclipse phases of the α Dra system.

5.2. Light curve analysis

We performed the light curve analysis using the Wilson-Devinney (WD) code, first formulated by Wilson & Devinney (1971) and subsequently generalised to eccentric binaries, also implementing complementary RVs analysis (Wilson 1979). The WD code employs Roche equipotential surfaces to describe the shapes of stars forming a binary system and is commonly used for the analysis of various configurations of binary systems. In our analysis we utilised the latest public version of the WD code with designation WD2015 (Wilson & Van Hamme 2014), through a user-friendly designed graphical user interface GUI as well as a Python backend wrapper developed by Güzel & Özdarcan (2020).

We started to set up our initial binary model by taking into account the orbital and atmospheric parameters derived in the previous sections and reported in Tables 3 and 4. According to the iterative process described in Sect. 4.4, we fixed the precisely determined temperature of the primary star ($T_{\mathrm{eff,A}}$), the mass ratio (q), and the projected separation of the orbit ($A \sin i$). Without prior knowledge of these parameters it is impossible to break the degeneracy of the binary solutions, which are only sensitive to the ratio of the effective temperatures and radii and

to the relative separation. An initial set of orbital parameters to be adjusted was prepared from the astrometric and spectroscopic orbital solutions (the period P, time of periastron passage T_{pp}, eccentricity e, and an angle of periastron ω), and the effective temperature of the secondary component $T_{eff,B}$. The surface gravities of both components $\log g_{A,B}$ are also used for initial guesses of the surface potentials of the components, $\Omega_{A,B}$. In light curve modelling only the ratio of the effective temperatures, and not the temperatures themselves, can be determined, thus the effective temperature of the primary component $T_{eff,A}$ was fixed. This component is dominant in the spectra of α Dra, contributing the majority of the total flux of the binary system, and consequently its effective temperature is determined with high precision from the atmospheric analysis. In our initial runs we optimised a total of nine free parameters: P, T_{pp}, e, ω, $T_{eff,B}$, Ω_A, Ω_B, fractional light contribution of primary star L_A, and inclination angle of the binary orbit i. Because WD2015 does not contain the TESS photometric bandpass, the Cousins I_c bandpass was used instead since its transmission is very close to that of TESS. The linear limb-darkening law was used with the coefficients interpolated from the tables of van Hamme (1993) with a WD2015 built-in subroutine. The gravity-brightening coefficient 0.25 for radiative atmospheres was applied after seminal derivation by von Zeipel (1924).

α Dra is a highly eccentric system ($e = 0.423$) with a long orbital period resulting in very short eclipses that cover only about 2.5% of the orbital cycle. In such cases, outside-of-eclipse measurements would be too heavily weighted in the light curve modelling. To suppress this unwanted effect, the TESS photometric observations were resampled; only each tenth measurement in the out-of-eclipse portions of the light curves is stored, whilst all the observations in the eclipses are used. This reduces significantly the number of observations that are employed in the light curve modelling. In total, for all five sectors of the TESS observations of α Dra (Fig. 9), 15187 measurements survived our selection which constitute about 16.5% of the initially extracted photometric measurements. We also increased the surface resolution to 60×60 (i.e. N1 and N2 parameters of WD2015) to make sure the required level of precision is achieved for modelling small-amplitude variations outside the eclipses (see below).

In the initial analysis, we detect sub-millimag level discrepancies in the descending branches of the secondary eclipses. Since the ascending and descending branches of the primary eclipses are in perfect agreement except for the depth in the last observed (third) primary eclipse, which is about 1 millimag deeper than in the previous two, we concluded that the orbital period is determined correctly. At present, it is not clear whether the effect seen in the secondary eclipses is real or instead is associated with some instrumental and/or data processing effects. To avoid any mix-up, we decided to perform the light curve analysis based separately on two observing parts so that the results can ultimately be examined for consistency. This way, the nearly continuous observations in Sectors 14, 15, and 16 comprise the 'Part 1' data set (9042 measurements), while the observations in Sectors 21 and 22 comprise the 'Part 2' data set (6145 measurements). This division is also indicated in Fig. 9, which shows raw TESS observations for all five sectors separately.

α Dra is a partially eclipsing system, as is obvious from the characteristic V shape of its light curve minima. Therefore, degeneracies and correlations of the parameters in a multi-dimensional parameter space are expected (Conroy et al. 2020). To explore the parameter space, and to obtain error estimates, many researchers utilise Markov chain Monte Carlo (MCMC;
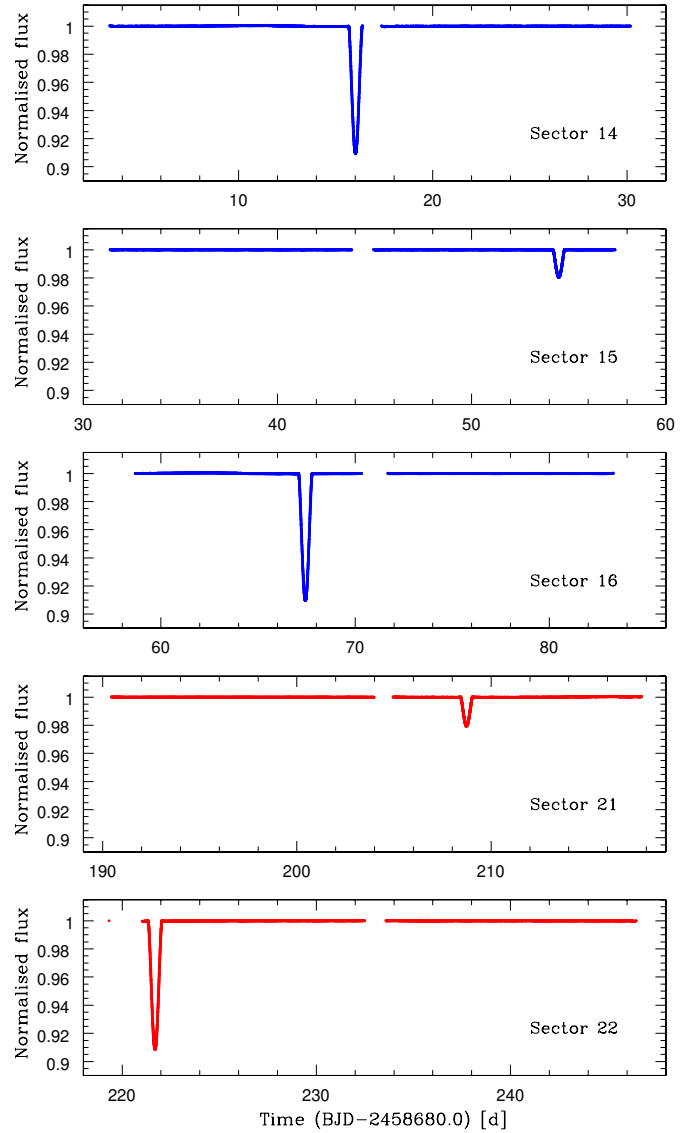

Fig. 9. TESS photometric measurements of α Dra: normalised flux as a function of time, where $t = 0$ is for BDJ 2 458 680.0 d. The light curve analysis presented in Sect. 5.2 was performed separately for the observations in Sectors 14, 15, and 16 (Part 1, in blue), and Sectors 21 and 22 (Part 2, in red).

Goodman & Weare 2010) optimisers (e.g., Lehmann et al. 2020, Dervişoğlu et al. 2018). For the purpose of optimising the nine free parameters mentioned above, we developed a PYTHON framework (Lc$_{MCMC}$) that uses PyWD2015 (Güzel & Özdarcan 2020) as a WD backend and the widely used EMCEE package (Foreman-Mackey et al. 2013) as an ensemble sampler.

To obtain a good fit we sampled parameter priors with a normal distribution around 10% To guarantee the convergence, we used the integrated auto-correlation time module of EMCEE to assure that enough number iterations had been achieved. Our final MCMC solution yielded approximately 200 000 iterations for each part of the photometric data through 64 walkers.

In Table 5 we list the results of the posterior probability distributions of the optimised parameters. We calculated the relative radii $r_{A,B}$, surface gravities $\log g_{A,B}$, and the light ratio ℓ_B/ℓ_A, accordingly. The reported uncertainties and mean values were calculated from the 16th, 50th, and 84th percentiles of each distribution. For the adopted values, we assumed symmetric errors
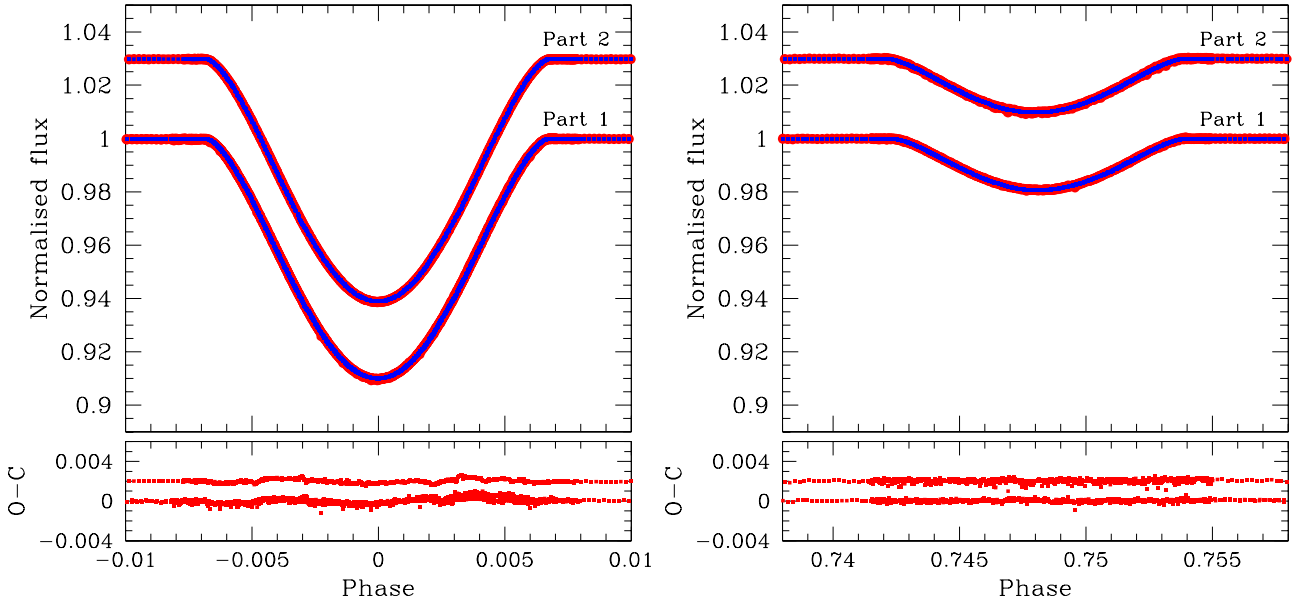
Fig. 10. Fits to the TESS light curve of α Dra for the primary (*left*) and secondary (*right*) minima. The normalised TESS measurements (*upper panels*) and O-C residuals (*lower panels*) are shown as red symbols, while the best fit obtained with the WD code is illustrated as a blue solid line (see text for definition of Part 1 and Part 2 light curves). The phases are calculated from the ephemeris determined from the observed primary minima, $T_{\mathrm{pr.\,min}} = (2458696.01948 \pm 0.00003) + (51.41891 \pm 0.00011)\,E$. The light curves and best fit, and the residuals, for Part 2 are arbitrarily shifted upwards for better visibility.

which is also the core assumption of the normal distributions (last column in Table 5).

The best fit models are shown for the primary and secondary minima in both Part 1 and Part 2 data sets in Fig. 10. We also illustrate the accuracy of our models that successfully fitted the 1 millimag level of the out-of-eclipse brightening, as shown in Fig. 11. The corner plots of the samples in the marginalised posterior distributions of each part of the photometric data are also shown in Appendix B (Figs. B.1 and B.2). The obvious correlation between the optimised parameters demonstrates the importance of adopting stochastic methods such as Bayesian inference for the multi-parameter model estimations.

It is evident from Figs. 10 and 11 that the decision to analyse the TESS light curves from Sectors 14, 15, and 16 (Part 1) and Sectors 21 and 22 (Part 2) separately is fully justified. There are no systematics in the residuals between the best fitting calculated light curves and observations in the secondary minima, whilst the residuals are in sub-millimag level (right panel in Fig. 10). The same is true for the proximity (reflection) light excess at the orbital phases from 0.80 to 0.99 (Fig. 11). The residuals from fitting two primary minima in Part 1 and one primary minimum in Part 2 are somewhat larger, yet the amplitude does not exceed the 1 millimag level (see left panel in Fig. 10). A comparison between the Part 1 and Part 2 light curve solutions reveals a high degree of consistency within the quoted 1σ uncertainties for all inferred parameters (see Table 5).

Orbital parameters inferred from interferometric, spectroscopic, and photometric data are listed in Tables 2, 3, and 5, respectively. Four parameters are in common between these determinations: the orbital period P, time of periastron passage T_{pp}, orbital eccentricity e, and argument of periastron ω. The first three parameters are found to be in good agreement within the quoted 1σ uncertainties, while ω inferred from the interferometric data is 2σ away from the respective values deduced from the spectroscopic and photometric data. Furthermore, the orbital inclination obtained in the astrometric analysis is also 2σ away from the value inferred from photometry. However, we note that
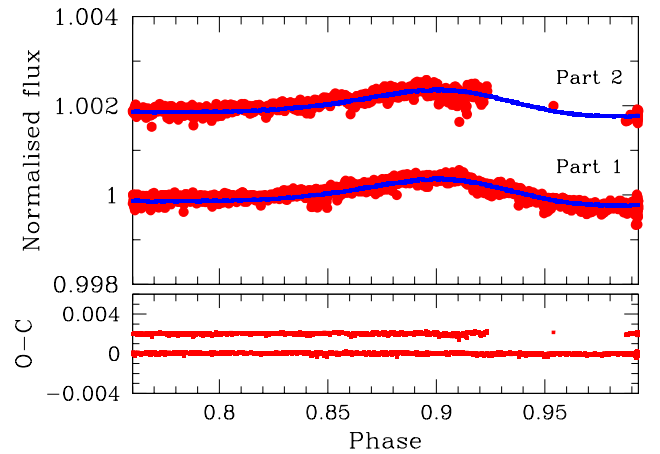

Fig. 11. Same as Fig. 10, but in the portion of the light curve preceding the primary minimum. Brightening due to the proximity effect (reflection) is well below 1 millimag level, and is detected only thanks to the superb high-precision space photometry acquired by the TESS mission. The light curves and best fit for the Part 2 are arbitrarily shifted upwards for better visibility.

the astrometric value has an uncertainty that is an order of magnitude larger. For that reason we use the orbital inclination value of $i = 86°.352 \pm 0°.025$, as inferred from the light curve solution, for the final determination of physical properties of the stars and for the dynamical parallax of the system.

6. Evolutionary models

The combined spectroscopic, photometric, and astrometric analyses described in the previous sections allows us to put both components of the α Dra system in the log T_{eff}–log g Kiel diagram and to assess its evolutionary status. We closely followed the procedure outlined in Tkachenko et al. (2020) that makes

Table 3. Orbital parameters of the α Dra system, obtained via the spectral disentangling method, from 46 high-resolution high S/N H$\textsc{ermes}$ spectra.

Parameter	Unit	Value
P	[d]	51.41891 (fix)
T_{pp}	[d]	$2\,451\,441.804 \pm 0.014$
e		0.4229 ± 0.0012
ω	[deg]	21.28 ± 0.13
K_A	[km s^{-1}]	48.512 ± 0.054
K_B	[km s^{-1}]	63.58 ± 0.41
q		0.7642 ± 0.0064
$M_A \sin^3 i$	[$M_\odot$]	3.167 ± 0.044
$M_B \sin^3 i$	[$M_\odot$]	2.416 ± 0.019
$A \sin i$	[$R_\odot$]	103.19 ± 0.38

Notes. The orbital period was fixed to the value determined from the observed primary minima (see Sect. 5). The uncertainties in the orbital parameters were calculated with the bootstrapping method from 10 000 samples.

use of a grid of Modulus for experiments in stellar astrophysics M$\textsc{esa}$ stellar structure and evolution models (Paxton et al. 2011, 2013, 2015, 2018, 2019), as presented in Johnston et al. (2019b). The grid employs the Ledoux criterion for convection and assumes a chemical mixture after Przybilla et al. (2008) and Nieva & Przybilla (2012) (also known as the cosmic abundance standard). We set the initial hydrogen and helium fractions to $X = 0.710$ and $Y = 0.276$, respectively, and the mixing-length parameter α_{mlt} to the solar calibrated value of 1.8. In addition, the grid employs a mixing profile in the radiative envelope determined by Rogers & McElwaine (2017) from 2D hydrodynamical simulations of internal gravity waves and implemented in M$\textsc{esa}$ by Pedersen et al. (2018). Overall, the grid of Johnston et al. (2019b) is optimised for intermediate-mass stars born with a convective core, which makes it an excellent tool for the evolutionary analysis of the α Dra system.

Figure 12 shows the results of fitting M$\textsc{esa}$ evolutionary tracks to the positions of both binary components in the Kiel (left column) and HR (right column) diagrams. The positions of both components (black circle and square for the primary and secondary, respectively) are well reproduced within 1σ uncertainties of the measured effective temperatures, surface gravities, and luminosities of the stars (see Table 6 for numerical values) and assuming their dynamical masses (solid black tracks in Fig. 12). For the secondary component we also considered a second scenario corresponding to its spectroscopic value of T_{eff} (see Table 4, column '2b', for numerical value and blue square in Fig. 12). The best fit solution (solid blue track in Fig. 12) is obtained for the stellar mass that is approximately 3% larger than the inferred dynamical mass of the star. However, owing to the large spectroscopic ΔT_{eff} of 250 K, the corresponding position of the secondary in the Kiel and HR diagrams is also consistent within 1σ uncertainty of the dynamical mass track of the star. For the primary component we find that a small amount of convective core overshooting cannot be excluded (solid red track in Fig. 12), although the $f_{\text{ov}} = 0.005$ track (corresponding to the lower boundary in the employed grid of M$\textsc{esa}$ models) is also consistent with the stellar position in the Kiel and HR diagrams.

In Table 6, we list the final accepted parameters (age, mass of the convective core, and overshooting parameter) inferred from our evolutionary analysis. We note that the parameters are based

on the effective temperature and luminosity of the secondary inferred from the TESS light curve. As discussed in detail in Sect. 4.4, owing to a small contribution of the secondary component to the composite spectrum of the binary system, its disentangled spectrum is significantly more uncertain than that of the primary component. In particular, we found that the Balmer lines were considerably affected in the disentangling process and hence could not be used in the spectroscopic analysis. That being said, the quality of the spectroscopic information that we have at our disposal for the secondary component is inferior to the quality of the TESS light curve of the system, hence we put more trust in the photometrically inferred $\log T_{\text{eff}} / \log L$ pair for the secondary component. According to our findings, the primary component is an evolved post-TAMS[3] A-type star that has a tiny convective core ($M_{cc} = 0.01 \pm 0.04$). On the other hand, the secondary component is a relatively unevolved star whose convective core mass constitutes approximately 14% of the stellar mass. We estimated the age of the system to be about 300 Myr, with the individual ages being 280 ± 10 and 345 ± 25 Myr for the primary and secondary component, respectively. We note that the individual ages are in a good agreement with each other within 2σ uncertainties, and the difference between them reduces to within 1σ when the spectroscopic T_{eff} value of 10165 ± 250 K is assumed for the secondary (age and convective core mass of the star respectively 315 ± 22 Myr and $M_{cc} = 0.354 \pm 0.010\,M_\odot$ in this case).

Another test could be made to verify consistency between the light ratio determined from the observables ($\ell_B/\ell_A = 0.212 \pm 0.014$) in the TESS passband and the light ratio inferred from the evolutionary tracks for determined dynamical masses of the components. The M$\textsc{esa}$ isochrones & stellar tracks M$\textsc{ist}$ interactive tool (Dotter 2016; Choi et al. 2016; Paxton et al. 2011, 2013, 2015, 2018, 2019) provided the synthetic photometry for the M$\textsc{esa}$ models for the various photometric passbands. First, we compared the evolutionary tracks for the components from our grid and the M$\textsc{ist}$ calculations, and found an excellent matches. Then for the TESS passband the calculations give the light ratio $(\ell_B/\ell_A)_{\text{MESA}} = 0.221 \pm 0.015$, which is within 1σ uncertainty of the light ratio determined in the light curve analysis.

In this context we should mention that the calculation of the light ratio in the B and V passbands (the spectral range in which our spectroscopic analysis was performed) corroborate our previous assumption that the change with wavelength is small, and within the uncertainties of our analysis: $(\ell_B/\ell_A)_B = 0.213 \pm 0.018$, and $(\ell_B/\ell_A)_V = 0.221 \pm 0.022$.

7. Distance to α Dra

Prior to the launch of astrometric space missions, the trigonometric parallax for α Dra was uncertain. The entry for its parallax in The General Catalogue of Trigonometric [stellar] Parallaxes (van Altena et al. 1995) reads $\pi = 14.8 \pm 7.5$ mas. On the other hand, the H$\textsc{ipparcos}$ parallax from the first 1997 reduction (Perryman et al. 1997) is $\pi_{\text{HIP}} = 10.56 \pm 0.52$ mas and provides a considerable improvement over the previously published measurement. Moreover, the improved H$\textsc{ipparcos}$ reduction from 2007 results in a slight increase in the absolute value of the parallax for α Dra and in a significant increase in the precision of the measurement: $\pi_{\text{HIP}} = 10.76 \pm 0.17$ mas (van Leeuwen 2007). Finally, the *Gaia* Data Release 2 (DR2) (Gaia Collaboration 2018) trigonometric parallax of $\pi_{Gaia} = 12.18 \pm 0.32$ mas is somewhat larger than the 2007

---

[3] Terminal age main sequence

Table 4. Atmospheric parameters of the two components of the α Dra system as inferred from their disentangled spectra with the GSSP_SINGLE module.

Parameter	Value ± Error		
	Run 1	Run 2a	Run 2b
		Primary	
$T_{\rm eff}$ (K)	10190 ± 125	10205 ± 100	$\mathbf{10225 \pm 100}$
$\log g$ (dex)	3.52 ± 0.09	$3.5511^{(*)} \pm 0.0081$	$\mathbf{3.5511^{(*)} \pm 0.0081}$
[M/H] (dex)	-0.03 ± 0.05	0.01 ± 0.05	$\mathbf{0.01 \pm 0.05}$
ξ (km s^{-1})	1.06 ± 0.21	1.26 ± 0.30	$\mathbf{1.34 \pm 0.30}$
$v \sin i$ (km s^{-1})	25.4 ± 0.7	25.4 ± 0.9	$\mathbf{25.4 \pm 0.9}$
light factor	0.848 ± 0.012	0.83 ± 0.01	$\mathbf{0.825^{(*)} \pm 0.010}$
		Secondary	
$T_{\rm eff}$ (K)	——	10150 ± 300	$\mathbf{10165 \pm 250}$
$\log g$ (dex)	——	$4.095^{(*)} \pm 0.023$	$\mathbf{4.095^{(*)} \pm 0.023}$
[M/H] (dex)	——	-0.12 ± 0.15	$\mathbf{-0.01 \pm 0.09}$
ξ (km s^{-1})	——	0.1 ± 0.9	$\mathbf{0.75 \pm 0.75}$
$v \sin i$ (km s^{-1})	——	168 ± 10	$\mathbf{168 \pm 11}$
light factor	——	0.20 ± 0.02	$\mathbf{0.175^{(*)} \pm 0.011}$

Notes. The asterisk $(^*)$ refers to the parameters whose values are fixed to those inferred from the TESS light curve. The finally accepted set of parameters is highlighted in boldface.

Table 5. WD2015 best fit solutions for the TESS light curves of the α Dra system.

Parameter	Unit	Part 1 Sectors 14, 15, 16	Part 2 Sectors 21, 22	Adopted solution
Orbital elements				
Orbital period P	[d]	51.4198 ± 0.0031	51.4200 ± 0.0032	51.4199 ± 0.0031
Time of periastron $T_{\rm pp}$	[d]	2458753.107 ± 0.019	2458753.118 ± 0.026	2458753.112 ± 0.023
Eccentricity e		0.4230 ± 0.0013	0.4217 ± 0.0026	0.4223 ± 0.0021
Argument of periastron ω	[deg]	20.74 ± 0.53	20.27 ± 0.78	20.51 ± 0.67
Orbital inclination i	[deg]	86.345 ± 0.024	86.358 ± 0.026	86.352 ± 0.025
Stars				
Surface potential of star A $\Omega_{\rm A}$		22.22 ± 0.14	22.32 ± 0.16	22.27 ± 0.15
Surface potential of star B $\Omega_{\rm B}$		36.21 ± 0.80	35.90 ± 0.95	36.06 ± 0.88
Fractional radius of star A $r_{\rm A}$		0.0479 ± 0.0003	0.0476 ± 0.0004	0.0477 ± 0.0003
Fractional radius of star B $r_{\rm B}$		0.0224 ± 0.0005	0.0226 ± 0.0006	0.0225 ± 0.0005
Eff. temperature of star A $T_{\rm eff,A}$	[K]	$10\,225$ (fix)	$10\,225$ (fix)	$10\,225$ (fix)
Eff. temperature of star B $T_{\rm eff,B}$	[K]	$10\,031 \pm 248$	$9\,837 \pm 375$	9930 ± 328
Light of star A $L_{\rm A}$		101.61 ± 1.44	100.61 ± 1.78	101.11 ± 1.62
Light of star B $L_{\rm B}$		21.57 ± 1.24	21.27 ± 1.49	21.42 ± 1.37
Fractional light of star A $\ell_{\rm A}$		0.8249 ± 0.0172	0.8255 ± 0.0214	0.8252 ± 0.0194
Fractional light of star B $\ell_{\rm B}$		0.1751 ± 0.0104	0.1745 ± 0.0126	0.1748 ± 0.0115
Light ratio $\ell_{\rm B}/\ell_{\rm A}$		0.2123 ± 0.0125	0.2114 ± 0.0152	0.2118 ± 0.0139

Notes. The adopted solution is reported in the last column and represents the mean of the two individual solutions (see text for definition of the Part 1 and Part 2 data sets).

HIPPARCOS value putting α Dra at a shorter distance ($d_{Gaia} = 82.1 \pm 2.1$ pc).

The *Gaia* Early Data Release 3 (EDR3) parallax for α Dra is $\pi_{\rm EDR3} = 12.516 \pm 0.203$ mas (Gaia Collaboration 2021), slightly larger than quoted in the *Gaia* DR2. The parallax uncertainty may be underestimated by $\approx 30\%$ as described in Sect. 6.3.1 of Gaia Collaboration (2021). The distance derived from the EDR3 parallax and published uncertainty is $d_{\rm EDR3} = 79.9 \pm 1.3$ pc, and considering the increased uncertainty it is $d_{Gaia} = 79.9^{+4.1}_{-3.7}$ pc. As seen in Fig. 13, this distance places α Dra closer than other distance determinations. The solution in EDR3 is a five-parameter solution, and *Gaia* does not yet provide solutions for binary stars.

There are hints within the statistics that α Dra might be resolved. The renormalised unit weight error (ruwe) is 2.4 and this is greater than the 1.4 level that may indicate a resolved double. However, the related statistic ipd_gof_harmonic_amplitude is 0.056, which is less than the 0.1 associated with resolved doubles (Gaia Collaboration 2021). If α Dra were resolved by *Gaia*, the PSF should be elongated along the position angle of the binary at epoch 2016.0, the epoch of EDR3 (Gaia Collaboration 2021; Fabricius et al. 2021). The statistic ipd_gof_harmonic_phase is 108°.091. For the orbital elements in Table 2 the predicted ephemeris gives a position angle of 252°.76 and a separation of 7.4 mas. As the phase

Table 6. Stellar properties of the components in the binary system α Dra determined from the combined spectroscopic and light curve analysis, and evolutionary calculations.

Parameter	Unit	Primary	Secondary
M	$[M_\odot]$	3.186 ± 0.044	2.431 ± 0.019
R	$[R_\odot]$	4.932 ± 0.036	2.326 ± 0.052
$\log g$	[dex]	3.555 ± 0.006	4.090 ± 0.019
T_{eff}	[K]	$10\,225 \pm 100$	$9\,930 \pm 330$
$\log L$	$[L_\odot]$	2.380 ± 0.018	1.677 ± 0.059
M_{bol}	[mag]	-1.200 ± 0.045	0.557 ± 0.147
$v \sin i$	[km s^{-1}]	25.4 ± 0.9	168 ± 11
Age	[Myr]	280 ± 10	345 ± 25
M_{cc}	$[M_\odot]$	0.01 ± 0.04	0.337 ± 0.011
X_c		0.00 ± 0.005	0.41 ± 0.03
f_{ov}		0.007 ± 0.002	0.005 [*]

Notes. [*]The secondary component is not sufficiently evolved to deduce its overshooting parameter from the Kiel or HRD diagram, hence f_{ov} is fixed to 0.005 H_p.

of the PSF elongation is modulo 180° the rotated ephemeris position angle to consider is 72°.76. This is offset from the `ipd_gof_harmonic_amplitude` by 31°. Until a binary solution from *Gaia* is provided it is speculative to associate this 31° offset for a 7 mas binary with the flux ratio determined in this work. In summary, there are two statistics suggestive of a resolved binary: `ruwe` and `ipd_gof_harmonic_phase`. Although, it is not clear that the orientation of the phase supports agreement with the position angle of the binary at this time. The `ipd_gof_harmonic_amplitude`, which should be considered with the `ruwe`, does not suggest a resolved binary. We eagerly await future releases from *Gaia* that include results for resolved doubles.

Our complementary observations of the α Dra system enable direct determination of its distance through the measurements of the angular semi-major axis of the orbit a'' (see Table 2) and the semi-major axis of the spectroscopic orbit (see Table 3). With $A \sin i = 103.37 \pm 0.49\,R_\odot$, $a'' = 5.52 \pm 0.06$ mas, and $i = 86.35 \pm 0.03$ deg inferred from interferometry, spectroscopy, and combined spectroscopic and photometric analysis, respectively, we obtain a distance to the α Dra binary system of $d = 87.07 \pm 1.03$ pc, or expressed as the dynamical parallax $\pi_{\text{dyn}} = 11.48 \pm 0.13$ mas. Figure 13 provides a graphical representation of the comparison of the distance derived in this work with the distances inferred from the HIPPARCOS and *Gaia* parallaxes.

The distance to a binary system can also be derived from stellar luminosities and the measured apparent brightness, provided the fractional light contribution of each component to the total light of the binary system is known. Since the individual radii, effective temperatures, and fractional light contributions of the components are determined in the present analysis, we can also provide alternative distance estimates to the system. Oja (1993) measured the BV brightness of α Dra to be $B = 3.640 \pm 0.007$ mag and $V = 3.680 \pm 0.009$ mag. Absolute bolometric magnitudes M_{bol}, also given in Table 6, are transformed to absolute visual magnitudes M_V, hence the bolometric correction BC_V are applied. Here we use the bolometric corrections from four different sources: empirical tabulation from Code et al. (1976) and Flower (1996)[4], and theoretical estimates from model

---
[4] See corrections given in Torres (2010).

atmospheres for given photometric bandpasses by Bessell et al. (1998) and Girardi et al. (2002). We use an estimate of the colour excess for α Dra $E(B-V) = 0.025$ from Zorec et al. (2009) who compute it as an average from several independent determinations with different methods. In Kervella et al. (2019) a somewhat lower colour excess of $E(B-V) = 0.007$ is reported using an interactive code STILSM which implements 3D maps of the local ISM (Lallement et al. 2014, 2018). Our calculations were performed with the code JKTABSDIM (Southworth et al. 2005) where in addition to the parameters listed above we also assume interstellar absorption. Taking interstellar attenuation of light into account resulted in shorter distances compared to the case when the effect is ignored.

Calculations of the distance to α Dra using the stellar properties of its components determined in the present work eventually give two groups of results, clustered at a 'short' distance of $d \sim 90$ pc, and at a 'long' distance of $d \sim 100$ pc. None of our estimates are in agreement with the *Gaia* parallax-based distance measurement, while some overlap within 1σ uncertainties is obtained with the HIPPARCOS parallax-based distance determinations (see Fig. 13). We note that among the different calibrations of the bolometric corrections, the empirical tabulation given by Flower (1996) gives the distance $d_{\text{FLO,V}} = 87.8 \pm 2.5$ pc, which is in a good agreement within the quoted 1σ uncertainty with the distance measured from the dynamical parallax in this work. We also note that the *Gaia* parallax measurement did not take into account that α Dra is a binary system, hence the corresponding distance estimate is expected to be uncertain.

A group of the long distance determinations comprises distances determined from the theoretical bolometric corrections, those of Girardi et al. (2002) being close to distance of 100 pc, $d_{\text{GIR,B}} = 95.8 \pm 2.6$ pc and $d_{\text{GIR,V}} = 98.7 \pm 2.7$ pc, while application of the theoretical bolometric corrections from Bessell et al. (1998) gives the largest distance of all, $d_{\text{BES,V}} = 99.9 \pm 2.7$ pc. The largest distance came for the empirical calibration given by Code et al. (1976), $d_{\text{COD,V}} = 99.8 \pm 3.7$ pc, also with the largest uncertainty. Distances quoted are for the calculations of the binary system as a whole. With a prevailing flux coming from the primary component, less precisely determined physical properties of the secondary component have no decisive role in the error budget in distance determinations.

The MIST interactive tool using the MESA models we use in this work also provide synthetic photometry with built-in bolometric corrections. This enables calculations of the absolute magnitudes in a given photometric passband. The absolute magnitudes in B and V passbands calculated for the MESA models with the physical quantities given in Table 6 are $M_B = -1.195$ mag, and $M_V = -1.134$ mag. Using the photometry for α Dra from Oja (1993), and $E(B-V) = 0.075$ from Zorec et al. (2009), the inferred distance to α Dra is $d_{\text{MESA,B}} = 88.4 \pm 2.3$ pc and $d_{\text{MESA,V}} = 88.6 \pm 2.4$ pc. This is close to the distance we determined from dynamical parallax, and to the distance calculated with the bolometric correction from Flower (1996), as represented in Fig. 13.

8. Summary and discussion

The detailed analysis of the newly obtained high-resolution high S/N HERMES optical spectra unambiguously reveals the spectral contribution of an A-type secondary component in the observed composite spectra of the α Dra system. The companion star is found to contribute approximately 17.5% of the total flux of the system; however, its rapid rotation implied by $v \sin i$ of 168 ± 11 km s^{-1} results in the apparent spectral contribution of
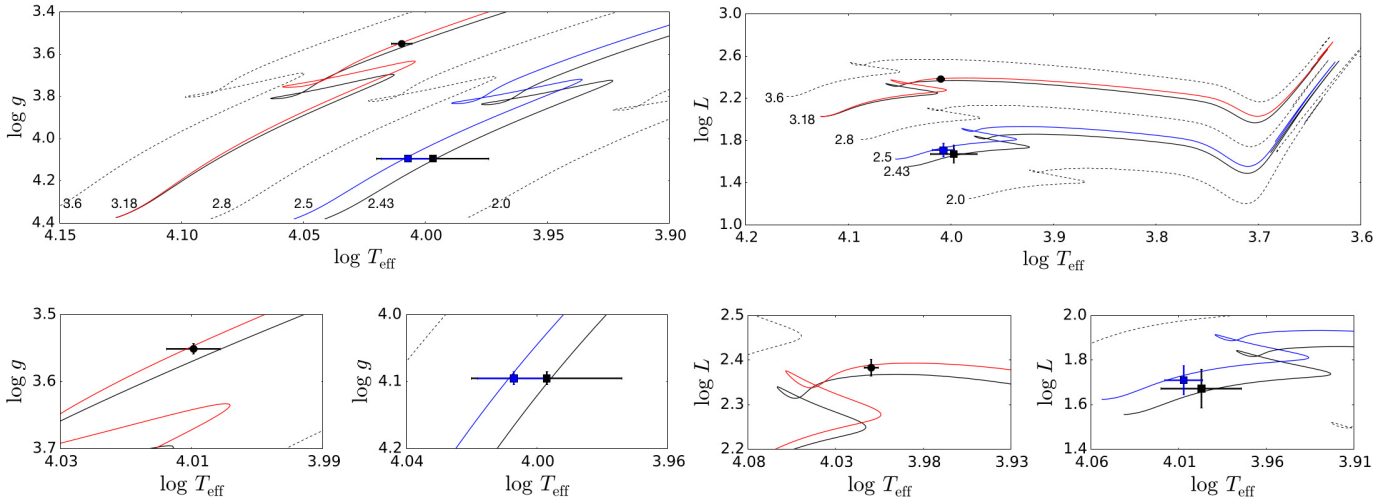
Fig. 12. *Top*: positions of the primary (circle) and secondary (squares) components of α Dra in the Kiel (*left column*) and HRD (*right column*) diagrams. The black and blue squares indicate the position of the secondary component corresponding respectively to its photometric and spectroscopic value of $T_{\rm eff}$. The MESA evolutionary tracks are shown as lines; the exact values of the stellar mass (in $M_\odot$ units) are indicated in the plot. The black solid lines correspond to the dynamical masses of the stars and are computed for the overshooting parameter $f_{\rm ov} = 0.005\,H_{\rm p}$. The blue track is the best fit to the spectroscopic $T_{\rm eff}$ of the secondary; the red line indicates a MESA evolutionary track corresponding to the dynamical mass of the primary component and computed with $f_{\rm ov} = 0.010\,H_{\rm p}$. *Bottom*: close-ups of the primary (*left*) and secondary (*right*) components of the binary systems.
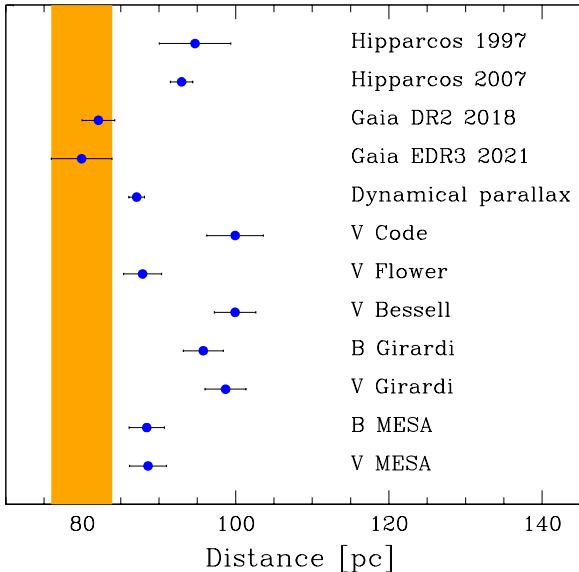

Fig. 13. Dynamical parallax of the binary system α Dra determined in this work compared to the trigonometric parallaxes measured by dedicated space astrometric missions, HIPPARCOS, and *Gaia*. Distance determinations based on the geometric and radiative properties of the stars in α Dra using different bolometric corrections are also shown. The latest *Gaia* distance from the *Gaia* EDR3 is shown in the coloured strip for easy comparison.

only 1% of the continuum level in the regions of metal lines. Therefore, it does not come as a surprise that α Dra has long been classified in the literature as a SB1 system. Our newly obtained data set also allows us to achieve the precision of ~0.1% in the measurement of the primary's RV semi-amplitude. A similar precision has been achieved by Kallinger et al. (2004) and Hey et al. (2022), while other measurements available in the literature are significantly inferior (e.g., Elst & Nelles 1983; Bischoff et al. 2017).

The combined analysis of the HERMES high-resolution spectroscopic data and the high-quality TESS space-based photometric data enabled us to determine the fundamental and atmospheric properties of both components of the α Dra system with high confidence. The precision achieved for the mass, radius, and effective temperature of the primary (secondary) component are approximately 1.4% (0.8%), 1.1% (3.1%), and 1.0% (3.0%). We find the mass and radius of the primary component to be respectively 14% and 15% lower than the values of $3.7 \pm 0.1\,M_\odot$ and $5.8 \pm 0.1\,R_\odot$ reported by Hey et al. (2022). We note that the α Dra system will be re-observed by the TESS mission during Sectors 48 and 49[5] of the cycle 4 observations, offering a prospect for further improvement in the above-mentioned precision, in particular for the radius of the secondary component.

The primary component of the α Dra system is an evolved A-type star, which is an extremely rare case when it comes to eclipsing double-lined binaries. Querying DEBCat[6], an online catalogue of detached eclipsing binaries with masses and radii determined with a precision better than 2% (maintained and regularly updated by Southworth 2015), results in only one binary system with an evolved A-type star, namely ψ Cen. This binary system comprises a pair of A0 IV and A1 V stars that reside in a 38.8 d orbit. Fundamental and atmospheric properties of both components of the ψ Cen system have been determined with high precision, thanks to the available WIRE space-based photometric (Bruntt et al. 2006) and ground-based high-resolution spectroscopic data (Mantegazza et al. 2010; Gallenne et al. 2019). For example, Gallenne et al. (2019) report the mass and radius of the primary component of ψ Cen to be $M = 3.187 \pm 0.031\,M_\odot$ and $R = 3.814 \pm 0.007\,R_\odot$. Therefore, the primary components of the ψ Cen and α Dra are strikingly similar in terms of their masses, while the difference of about $1\,R_\odot$ in their radii (see Table 6 for the parameters of α Dra) indicates that the primary component of α Dra is evolutionarily more advanced. This in turn suggests

---

[5] α Dra was also observed by the TESS mission during Sector 41; however, only out-of-eclipse phases were covered during the 27.4 days of observations.

[6] https://www.astro.keele.ac.uk/jkt/debcat/

a slight difference in the ages of the two systems, and indeed we find α Dra to be 310 ± 25 Myr old, which is to be compared to the age determinations of ψ Cen of $\tau(\psi$ Cen A$) = 280 \pm 10$ Myr (Gallenne et al. 2019) and $\tau(\psi$ Cen$) \sim 290$ Myr (Bruntt et al. 2006). Looking for 'a replica' of the secondary component of α Dra in terms of mass and age, the closest matches are the TZ Men A (Andersen et al. 1987) and V541 Cyg A (Torres et al. 2017) systems. Their masses and surface gravities (used as a proxy for age) match the respective quantities of α Dra B within $0.1\,M_\odot$ and 0.1 dex.

Royer et al. (2007) report a bi-modal distribution of the projected rotational velocity $v \sin i$ in early A-type stars, with slowly and rapidly rotating stars having distributions centred at $45\,\mathrm{km\,s^{-1}}$ and $200\,\mathrm{km\,s^{-1}}$, respectively. It is thus not unexpected to find a binary system composed of two early A-type stars with significantly different projected rotational velocities, especially when one of the components is at an advanced evolutionary stage. Our measurement of $v \sin i$ for the primary component is in excellent agreement with the value of $v \sin i = 25 \pm 2\,\mathrm{km\,s^{-1}}$ inferred by Royer et al. (2002) with the Fourier method. The projected rotational velocity of the secondary component of $168 \pm 11\,\mathrm{km\,s^{-1}}$ determined by us corroborates well the speculation by Hey et al. (2022) that a companion star must be a rapidly rotating A-type star with $v \sin i \sim 200\,\mathrm{km\,s^{-1}}$. A-type stars with discordant projected rotational velocities measured from different spectral lines were identified in observational studies by Zverko et al. (2011, 2018) and Vaňko et al. (2020), and references therein. Systematic spectroscopic observations revealed that this disparity in $v \sin i$ is a consequence of binarity itself, and the α Dra system adds extra value to that argument.

The angular diameters of both components of the α Dra binary system were resolved in our high angular resolution interferometric observations with the NPOI. The measured angular diameters for the primary and secondary components are $\theta_A = 0.62 \pm 0.05$ mas and $\theta_B = 0.28 \pm 0.05$ mas, respectively. Combining angular diameters with the dynamical parallax of $\pi = 11.48 \pm 0.13$ mas ($d = 87.07 \pm 1.03$ pc; see Sect. 7), we obtain linear radii of $R_{\mathrm{lin,A}} = 5.80 \pm 0.47\,R_\odot$ and $R_{\mathrm{lin,B}} = 2.62 \pm 0.47\,R_\odot$ for the primary and secondary component, respectively. We note that uncertainties in the interferometric measurements are the main contributor to the total error budget of the linear radii. The above-mentioned values are within 2σ, in agreement with the radius for the primary, and 1σ for the radius of the secondary component inferred from the combined spectroscopic and light curve analysis.

The high precision achieved in the measurement of the dynamical parallax of the system in turn leads to the 1.1% uncertainty on its distance. The distance from *Gaia* EDR3 trigonometric parallax is about 7 pc shorter than the value derived from our dynamical parallax. Due to the brightness of α Dra, the uncertainties of *Gaia* parallax when corrected are large and within 2σ, in agreement with our dynamical parallax. At the same time, inference of the distance to α Dra from physical properties of the components derived in this work (radii, effective temperatures, and accounting for the light ratio between the two components) and bolometric corrections gave a broad range of results. The closest distance to our measurement of the dynamical parallax is obtained from the empirical bolometric correction by Flower (1996), $d_{\mathrm{FLO}} = 87.9 \pm 2.5$ pc. On the other hand, using theoretically calculated bolometric corrections from Bessell et al. (1998) and Girardi et al. (2002) both yield a distance that is about 10 pc further away than the distance obtained in this work (see Fig. 13). We attribute the difference between the *Gaia* and dynamical

parallaxes to the (current) neglect of binarity in the *Gaia* solution, where the orbital movement produces changes in the photocentre of the star, and thus affects the determination of the trigonometric parallax, and also produces anomalous proper motion.

Inspired by the results of Hey et al. (2022) who reported a complex abundance pattern for the primary component of α Dra, we inferred abundances of helium, silicon, and scandium to check whether they are consistent with the solar metallicity of the star inferred from its disentangled spectrum. We focus here on He, Si, and Sc as these three elements are reported by Hey et al. (2022) to show some of the largest underabundances, while a detailed chemical composition analysis of both components of α Dra is the subject of a forthcoming paper. We confirm a slight underabundance of He (though consistent with the solar composition within the quoted errors) at the level of 0.1 ± 0.1 dex, whereas abundances of Si and Sc are found to be in excellent agreement with the deduced solar metallicity of the star. Hence, we speculate that the complex abundance pattern reported by Hey et al. (2022) for the primary component from the analysis of a co-added SOPHIE spectrum is a consequence of unaccounted spectral contribution of the secondary component to the observed composite spectrum of the system. Analysis of the spectrum of α Dra as if it were a single star is also likely the reason why Andersen et al. (1987) and Adelman et al. (2001) classified the system as a λ Boo chemically peculiar star. These stars are known for their metal deficiency, an effect that is easily mimicked by light dilution from an unseen companion in spectroscopic data.

Finally, from an evolutionary analysis of the system, we find that the primary component of α Dra is an evolved post-TAMS A-type star. The secondary component is shown to be relatively unevolved; its convective core mass constitutes about 14% of the apparent mass of the star. Fundamental and atmospheric properties of both binary components are consistent with low values of the convective core overshooting, with f_{ov} just below $0.010\,H_{\mathrm{p}}$.

9. Conclusion and future work

The analysis of α Dra presented in this work builds upon two fundamental findings in the literature: (i) spatially resolving the binary components based on the high-resolution NPOI interferometric data (Hutter et al. 2016), and (ii) detection of eclipses in TESS space-based photometric data (Bedding et al. 2019). Both these data sets suggest that α Dra is unlikely to be a SB1 system as previously reported in the literature, where Hutter et al. (2016) give an estimate of the light ratio of the two stars of about 0.19. Intrigued by the fact that such a rare system with an evolved A-type primary component has been spectroscopically misclassified as a SB1, due to a low apparent contribution of the secondary, we collected a new data set of high-resolution high S/N optical spectroscopic data to attempt the spectroscopic detection of a companion star, and for detailed analysis of the system based on combined spectroscopic, interferometric, and photometric data sets. We report the first unambiguous detection of the secondary component in the α Dra system, which makes it an eclipsing spectroscopic double-lined (SB2) binary.

The main results and conclusions of our work are the following:

– The companion star is found to contribute approximately 17% of the total light of the system, with the apparent spectroscopic line depths of about 1% in metal line regions, owing to the high rotational velocity of the star;

- The dynamical masses and radii of the primary and secondary components are found to be $M_A = 3.186 \pm 0.044\,M_\odot$ and $R_A = 4.932 \pm 0.036\,R_\odot$, and $M_B = 2.431 \pm 0.019\,M_\odot$ and $R_B = 2.326 \pm 0.052\,R_\odot$, respectively. The high precision of these parameters, coupled with precise measurements of the effective temperature for both stars, allows us to constrain the evolutionary status of both components and the age of the system as a whole;
- We confirm that the primary component is an evolved post-TAMS early A-type star. The companion, on the other hand, is a fairly unevolved main-sequence star whose convective core mass constitutes about 14% of its apparent total mass. The age of the system is estimated to be 310 ± 25 Myr;
- The high quality of our interferometric observations with an optimal distribution over the orbital cycle allow us to infer the angular semi-major axis with a precision of about 1%. This high precision in turn allows for the inference of a precise dynamical parallax of $\pi = 11.48 \pm 0.13$ mas, ultimately leading to the distance estimate of $d = 87.07 \pm 1.03$ pc.

Both components of the α Dra system are interesting targets to consider in the context of the mass discrepancy and near-core mixing levels in detached eclipsing double-lined binaries. The term mass discrepancy refers to the difference between the measured dynamical mass of the star and its mass that is inferred from fitting evolutionary models to the position of the star in the Kiel or HR diagram. Until recently, it was common to associate the mass discrepancy with large amounts of the near-core mixing in the form of overshooting (e.g., Guinan et al. 2000; Pavlovski et al. 2009), hence the two effects are not totally disconnected. Claret & Torres (2019) report a sharp increase in the f_{ov} overshooting parameter up to a mass of approximately $2\,M_\odot$ and a subsequent levelling off at the value of approximately $0.017\,H_p$ beyond $2\,M_\odot$ and at least up to $4.4\,M_\odot$. On the other hand, Tkachenko et al. (2020) find that (i) the mass discrepancy is a strong function of the surface gravity of the star, while it does not show any dependence on the stellar mass itself; (ii) the mass discrepancy can be only partially explained by insufficient near-core mixing and convective core mass predicted by evolutionary models; (iii) there is evidence that the mass discrepancy is strongly connected with incorrect spectroscopic inference of the effective temperature of the star due to ignoring the contribution of the turbulent and radiative pressure in the stellar atmosphere. We note, however, that the study by Tkachenko et al. (2020) generally deals with higher mass stars, in the mass range between $4.5\,M_\odot$ and $17\,M_\odot$. Our evolutionary analysis of the α Dra system does not support the conclusion of Claret & Torres (2019) as to the dependence of the convective core overshooting parameter on stellar mass. We find low overshooting values well below $f_{ov} = 0.010\,H_p$ for both binary components, while according to the dynamical masses and empirical findings by Claret & Torres (2016) the stars should show significantly higher levels of core overshooting. Perfect agreement between the dynamical and evolutionary mass for the evolved primary component of α Dra is also seemingly in contradiction with the findings of Tkachenko et al. (2020) that evolved stars tend to show large values of the mass discrepancy. However, we note that both components of α Dra have substantially lower masses than the bulk sample studied by Tkachenko et al. (2020), hence we do not expect their T_{eff} inference be significantly influenced by the turbulent and/or radiative pressure in the stellar atmosphere. Therefore, α Dra provides an extra argument for the mass discrepancy in eclipsing binaries to be strongly connected with inferior modelling of stellar atmospheres in certain mass regimes, and probably less so with the predictive power of

evolutionary models as to the convective core mass and amount of near-core mixing.

Finally, by looking at abundances of He, Si, and Sc in the atmosphere of the primary component of α Dra, we find the former to be slightly underabundant, while the other two elements show abundances consistent with the solar metallicity of the star. This result suggests the primary component might be a chemically ordinary A-type star; however, a more in-depth chemical composition analysis is required before any firm conclusions can be drawn. Detailed chemical composition analyses of the two components of α Dra and a subsequent comparison of the inferred abundance patterns with predictions from stellar structure and evolution models are the subject of a forthcoming paper (Sahin et al., in prep.).

References

Adelman, S. J., Caliskan, H., Kocer, D., et al. 2001, A&A, 371, 1078
Aller, L. H., Appenzeller, I., Baschek, B., et al. 1982, Landolt-Börnstein: Numerical Data and Functional Relationships in Science and Technology - New Series " Gruppe/Group 6 Astronomy and Astrophysics " Volume 2 Schaifers/Voigt: Astronomy and Astrophysics/Astronomie und Astrophysik " Stars and Star Clusters/Sterne und Sternhaufen
Almeida, L. A., Sana, H., Taylor, W., et al. 2017, A&A, 598, A84
Andersen, J., Clausen, J. V., & Nordstrom, B. 1987, A&A, 175, 60
Armstrong, J. T., Mozurkewich, D., Rickard, L. J., et al. 1998, ApJ, 496, 550
Balona, L. A., Baran, A. S., Daszyńska-Daszkiewicz, J., & De Cat, P. 2015, MNRAS, 451, 1445
Banyard, G., Sana, H., Mahy, L., et al 2022, A&A, 658, A69
Bedding, T. R., Hey, D. R., & Murphy, S. J. 2019, Res. Notes Am. Astron. Soc., 3, 163
Bessell, M. S., Castelli, F., & Plez, B. 1998, A&A, 333, 231
Bischoff, R., Mugrauer, M., Zehe, T., et al. 2017, Astron. Nachr., 338, 671
Bodensteiner, J., Sana, H., Wang, C., et al. 2021, A&A, 652, A70
Bruntt, H., Southworth, J., Torres, G., et al. 2006, A&A, 456, 651
Choi, J., Dotter, A., Conroy, C., et al. 2016, ApJ, 823, 102
Claret, A., & Torres, G. 2016, A&A, 592, A15
Claret, A., & Torres, G. 2017, ApJ, 849, 18

Claret, A., & Torres, G. 2018, ApJ, 859, 100
Claret, A., & Torres, G. 2019, ApJ, 876, 134
Code, A. D., Bless, R. C., Davis, J., & Brown, R. H. 1976, ApJ, 203, 417
Cohen, R. E., Geller, A. M., & von Hippel, T. 2020, AJ, 159, 11
Conroy, K. E., Kochoska, A., Hey, D., et al. 2020, ApJS, 250, 34
Dervişoğlu, A., Pavlovski, K., Lehmann, H., Southworth, J., & Bewsher, D. 2018, MNRAS, 481, 5660
Dotter, A. 2016, ApJS, 222, 8
Drimmel, R., Cabrera-Lavers, A., & López-Corredoira, M. 2003, A&A, 409, 205
Duchêne, G., & Kraus, A. 2013, ARA&A, 51, 269
Elson, R. A. W., Sigurdsson, S., Davies, M., Hurley, J., & Gilmore, G. 1998, MNRAS, 300, 857
Elst, E. W., & Nelles, B. 1983, A&AS, 53, 215
Fabricius, C., Luri, X., Arenou, F., et al. 2021, A&A, 649, A5
Feiden, G. A., & Chaboyer, B. 2012, ApJ, 761, 30
Feiden, G. A., & Chaboyer, B. 2013, ApJ, 779, 183
Feiden, G. A., & Chaboyer, B. 2014, ApJ, 789, 53
Flower, P. J. 1996, ApJ, 469, 355
Foreman-Mackey, D., Hogg, D. W., Lang, D., & Goodman, J. 2013, PASP, 125, 306
Frankowski, A., Jancart, S., & Jorissen, A. 2007, A&A, 464, 377
Gaia Collaboration (Brown, A. G. A., et al.) 2018, A&A, 616, A1
Gaia Collaboration (Brown, A. G. A., et al.) 2021, A&A, 649, A1
Gallenne, A., Pietrzyński, G., Graczyk, D., et al. 2019, A&A, 632, A31
Girardi, L., Bertelli, G., Bressan, A., et al. 2002, A&A, 391, 195
Goodman, J., & Weare, J. 2010, Commun. Appl. Math. Comput. Sci., 5, 65
Gray, D. F. 2014, AJ, 147, 81
Guinan, E. F., Ribas, I., Fitzpatrick, E. L., et al. 2000, ApJ, 544, 409
Güzel, O., & Özdarcan, O. 2020, Contrib. Astron. Obs. Skalnate Pleso, 50, 535
Hadrava, P. 1995, A&AS, 114, 393
Harper, W. E. 1907, JRASC, 1, 237
Hensberge, H., Pavlovski, K., & Verschueren, W. 2000, A&A, 358, 553
Hey, D. R., Kochoska, A., Monier, R., et al. 2022, MNRAS, in press, https://doi.org/10.1093/mnras/stac020
Higl, J., & Weiss, A. 2017, A&A, 608, A62
Hummel, C. A., Mozurkewich, D., Armstrong, J. T., et al. 1998, AJ, 116, 2536
Hummel, C. A., Benson, J. A., Hutter, D. J., et al. 2003, AJ, 125, 2630
Hutter, D. J., Zavala, R. T., Tycner, C., et al. 2016, ApJS, 227, 4
Ilijic, S., Hensberge, H., Pavlovski, K., & Freyhammer, L. M. 2004, in Spectroscopically and Spatially Resolving the Components of the Close Binary Stars, eds. R. W. Hilditch, H. Hensberge, & K. Pavlovski, ASP Conf. Ser., 318, 111
Johnston, C., Pavlovski, K., & Tkachenko, A. 2019a, A&A, 628, A25
Johnston, C., Tkachenko, A., Aerts, C., et al. 2019b, MNRAS, 482, 1231
Kallinger, T., Iliev, I., Lehmann, H., & Weiss, W. W. 2004, in The A-Star Puzzle, eds. J. Zverko, J. Ziznovsky, S. J. Adelman, & W. W. Weiss, 224, 848
Kervella, P., Arenou, F., Mignard, F., & Thévenin, F. 2019, A&A, 623, A72
Kolbas, V., Pavlovski, K., Southworth, J., et al. 2015, MNRAS, 451, 4150
Kroupa, P., Tout, C. A., & Gilmore, G. 1993, MNRAS, 262, 545
Lallement, R., Vergely, J. L., Valette, B., et al. 2014, A&A, 561, A91
Lallement, R., Capitanio, L., Ruiz-Dern, L., et al. 2018, A&A, 616, A132
Lehmann, H., Dervişoğlu, A., Mkrtichian, D. E., et al. 2020, A&A, 644, A121
Lightkurve Collaboration (Cardoso, J. V. d. M., et al.) 2018, Lightkurve: Kepler and TESS time series analysis in Python (Astrophysics Source Code Library)
Luo, F., Zhao, Y. H., Li, J., Guo, Y. J., & Liu, C. 2021, Res. Astron. Astrophys., 21, 272
Makarov, V. V., & Kaplan, G. H. 2005, AJ, 129, 2420
Mantegazza, L., Rainer, M., & Antonello, E. 2010, A&A, 512, A42
Martinet, S., Meynet, G., Ekström, S., et al. 2021, A&A, 648, A126
Mayer, P., Harmanec, P., & Pavlovski, K. 2013, A&A, 550, A2
Monier, R. 2021, Res. Notes Am. Astron. Soc., 5, 163
Mowlavi, N., Barblan, F., Saesen, S., & Eyer, L. 2013, A&A, 554, A108
Mozurkewich, D., Armstrong, J. T., Hindsley, R. B., et al. 2003, AJ, 126, 2502
Murphy, S. J., Corbally, C. J., Gray, R. O., et al. 2015, PASA, 32, e036
Nieva, M. F., & Przybilla, N. 2012, A&A, 539, A143
Oja, T. 1993, A&AS, 100, 591
Pavlovski, K., & Hensberge, H. 2005, A&A, 439, 309
Pavlovski, K., & Hensberge, H. 2010, in Binaries - Key to Comprehension of the Universe, eds. A. Prša, & M. Zejda, ASP Conf. Ser., 435, 207

Pavlovski, K., Tamajo, E., Koubský, P., et al. 2009, MNRAS, 400, 791
Pavlovski, K., Southworth, J., & Tamajo, E. 2018, MNRAS, 481, 3129
Paxton, B., Bildsten, L., Dotter, A., et al. 2011, ApJS, 192, 3
Paxton, B., Cantiello, M., Arras, P., et al. 2013, ApJS, 208, 4
Paxton, B., Marchant, P., Schwab, J., et al. 2015, ApJS, 220, 15
Paxton, B., Schwab, J., Bauer, E. B., et al. 2018, ApJS, 234, 34
Paxton, B., Smolec, R., Schwab, J., et al. 2019, ApJS, 243, 10
Pearce, J. A. 1957, Publ. Dominion Astrophys. Obs. Victoria, 10, 331
Pedersen, M. G., Aerts, C., Pápics, P. I., & Rogers, T. M. 2018, A&A, 614, A128
Perryman, M. A. C., Lindegren, L., Kovalevsky, J., et al. 1997, A&A, 500, 501
Pols, O. R., Tout, C. A., Schroder, K.-P., Eggleton, P. P., & Manners, J. 1997, MNRAS, 289, 869
Przybilla, N., Nieva, M.-F., & Butler, K. 2008, ApJ, 688, L103
Raskin, G., van Winckel, H., Hensberge, H., et al. 2011, A&A, 526, A69
Ricker, G. R., Winn, J. N., Vanderspek, R., et al. 2014, in Space Telescopes and Instrumentation 2014: Optical, Infrared, and Millimeter Wave, eds. J. Oschmann, M. Jacobus, M. Clampin, G. G. Fazio, H. A. MacEwen, et al., SPIE Conf. Ser., 9143, 914320
Ricker, G. R., Winn, J. N., Vanderspek, R., et al. 2015, J. Astron. Telesc. Instrum. Syst., 1, 014003
Rogers, T. M., & McElwaine, J. N. 2017, ApJ, 848, L1
Royer, F., Grenier, S., Baylac, M. O., Gómez, A. E., & Zorec, J. 2002, A&A, 393, 897
Royer, F., Zorec, J., & Gómez, A. E. 2007, A&A, 463, 671
Sana, H., de Mink, S. E., de Koter, A., et al. 2012, Science, 337, 444
Sana, H., de Koter, A., de Mink, S. E., et al. 2013, A&A, 550, A107
Sana, H., Le Bouquin, J. B., Lacour, S., et al. 2014, ApJS, 215, 15
Schöller, M., Correia, S., Hubrig, S., & Ageorges, N. 2010, A&A, 522, A85
Schröder, C., & Schmitt, J. H. M. M. 2007, A&A, 475, 677
Serenelli, A., Weiss, A., Aerts, C., et al. 2021, A&ARv, 29, 4
Shao, M., Colavita, M. M., Hines, B. E., et al. 1988, A&A, 193, 357
Shorlin, S. L. S., Wade, G. A., Donati, J. F., et al. 2002, A&A, 392, 637
Shulyak, D., Tsymbal, V., Ryabchikova, T., Stütz, C., & Weiss, W. W. 2004, A&A, 428, 993
Simon, K. P., & Sturm, E. 1994, A&A, 281, 286
Smith, J. C., Stumpe, M. C., Van Cleve, J. E., et al. 2012, PASP, 124, 1000
Southworth, J. 2015, in Living Together: Planets, Host Stars and Binaries, eds. S. M. Rucinski, G. Torres, & M. Zejda, ASP Conf. Ser., 496, 164
Southworth, J., Maxted, P. F. L., & Smalley, B. 2005, A&A, 429, 645
Stelzer, B., Hummel, C. A., Schöller, M., Hubrig, S., & Cowley, C. 2011, A&A, 529, A29
Struve, O. 1955, S&T, 14, 461
Struve, O., Sahade, J., Lynds, C. R., & Huang, S. S. 1957, ApJ, 125, 115
Themeßl, N., Hekker, S., Southworth, J., et al. 2018, MNRAS, 478, 4669
Tkachenko, A. 2015, A&A, 581, A129
Tkachenko, A., Pavlovski, K., Johnston, C., et al. 2020, A&A, 637, A60
Torres, G. 2010, AJ, 140, 1158
Torres, G., Andersen, J., & Giménez, A. 2010, A&ARv, 18, 67
Torres, G., Sandberg Lacy, C. H., Pavlovski, K., et al. 2014, ApJ, 797, 31
Torres, G., McGruder, C. D., Siverd, R. J., et al. 2017, ApJ, 836, 177
Tsymbal, V. 1996, in M.A.S.S., Model Atmospheres and Spectrum Synthesis, eds. S. J. Adelman, F. Kupka, & W. W. Weiss, ASP Conf. Ser., 108, 198
van Altena, W. F., Lee, J. T., & Hoffleit, E. D. 1995, The General Catalogue of Trigonometric [stellar] Parallaxes (New Haven)
van Belle, G. T., Creech-Eakman, M. J., & Hart, A. 2009, MNRAS, 394, 1925
van Hamme, W. 1993, AJ, 106, 2096
Vaňko, M., Pribulla, T., Hambálek, Ľ., et al. 2020, Contrib. Astron. Obs. Skalnate Pleso, 50, 632
van Leeuwen, F. 2007, A&A, 474, 653
von Zeipel, H. 1924, MNRAS, 84, 665
White, T. R., Pope, B. J. S., Antoci, V., et al. 2017, MNRAS, 471, 2882
Wilson, R. E. 1979, ApJ, 234, 1054
Wilson, R. E., & Devinney, E. J. 1971, ApJ, 166, 605
Wilson, R. E., & Van Hamme, W. 2014, ApJ, 780, 151
Zorec, J., Cidale, L., Arias, M. L., et al. 2009, A&A, 501, 297
Zverko, J., Žižňovský, J., Iliev, I., et al. 2011, Astrophys. Bull., 66, 325
Zverko, J., Iliev, I., Romanyuk, I. I., et al. 2018, Astrophys. Bull., 73, 351

Appendix A: Interferometric observations of α Dra

Table A.1. Mark III (1989–1992) and NPOI (1997–2015) observations

UT Date (1)	Julian Year (2)	Triangles and baselines (3)	$B_{\min}[m]$ (4)	$B_{\max}[m]$ (5)	Calibrators (6)
1989 Apr 18	1989.2945	NF-SC	16	17	FK5 509
1991 Jun 19	1991.4627	NF-SC	14	17	FK5 913
1992 Feb 28	1992.1584	NF-SC	13	17	FK5 447 FK5 456
1992 Apr 28	1992.3225	NF-SD	19	20	HR 5062 FK5 447 FK5 509
1992 May 02	1992.3337	NC-SC	8	10	HR 5062 HR 5329 FK5 456
1992 Jun 08	1992.4349	NF-SC	12	17	HR 5062 FK5 456
1992 Jul 06	1992.5113	NA-SA	9	10	HR 5062
1997 Mar 19	1997.2125	AC-AE-AW	18	37	FK5 472
1997 Mar 26	1997.2318	AC-AE-AW	16	37	FK5 447 FK5 472
1997 Apr 15	1997.2864	AC-AE-AW	17	37	FK5 423 FK5 472
1997 Apr 18	1997.2946	AC-AE-AW	17	37	FK5 472
1997 May 08	1997.3493	AC-AE-AW	17	37	FK5 423 FK5 472 FK5 668
1997 May 29	1997.4067	AC-AE-AW	16	37	FK5 423 FK5 668
1997 Jun 19	1997.4640	AC-AE-AW	16	37	FK5 447 FK5 456 FK5 472 FK5 509 FK5 668
1997 Jun 21	1997.4695	AC-AE-AW	17	37	FK5 447 FK5 472 FK5 509
1997 Jun 22	1997.4723	AC-AE-AW	14	37	FK5 447 FK5 472 FK5 509 FK5 668
1997 Jun 26	1997.4834	AC-AE-AW	15	36	FK5 472 FK5 509 FK5 668
1997 Jun 27	1997.4859	AC-AE-AW	17	37	FK5 472 FK5 509
1997 Jul 04	1997.5051	AC-AE-AW	14	37	FK5 447 FK5 509
1997 Jul 08	1997.5159	AC-AE-AW	17	37	FK5 509 FK5 668
1997 Jul 09	1997.5188	AC-AE-AW	15	36	FK5 509
1997 Jul 13	1997.5298	AC-AE-AW	16	37	FK5 509
1997 Jul 14	1997.5325	AC-AE-AW	15	37	FK5 509
1997 Jul 18	1997.5435	AC-AE-AW	14	35	FK5 509
2013 Mar 05	2013.1743	AW-AC	19	53	FK5 0472
2013 Mar 06	2013.1769	AW-AC	19	53	FK5 0472
2013 Mar 07	2013.1797	AW-AC	19	53	FK5 472
2013 May 24	2013.3931	AW-AC	15	50	FK5 472
2013 May 25	2013.3956	AC-AW-E6	16	53	FK5 0472
2013 May 26	2013.3985	AW-AC	16	50	FK5 472
2013 May 27	2013.4012	AC-AW-E6	16	53	FK5 472
2013 May 30	2013.4094	AC-AW-E6	15	53	FK5 472
2013 May 31	2013.4121	AC-AW-E6	16	53	FK5 472
2013 Jun 01	2013.4148	AC-AW-E6	16	53	FK5 472
2013 Jun 03	2013.4203	AC-AW-E6	16	53	FK5 472
2013 Jun 04	2013.4230	AC-AW-E6	16	53	FK5 472
2013 Jun 05	2013.4258	AC-AW-E6	15	53	FK5 472
2013 Jun 07	2013.4315	AW-AC	15	50	FK5 472
2013 Jun 08	2013.4341	AW-AC	16	50	FK5 423 FK5 472
2013 Jun 10	2013.4395	AW-AC	15	50	FK5 423 FK5 472
2013 Jun 11	2013.4423	AW-AC	15	50	FK5 423 FK5 472
2013 Jun 13	2013.4477	AW-AC	17	51	FK5 423 FK5 472
2013 Jun 15	2013.4532	AW-AC	16	51	FK5 423 FK5 472
2013 Jun 16	2013.4559	AW-AC	16	51	FK5 423 FK5 472
2013 Jun 17	2013.4586	AW-AC	16	50	FK5 423 FK5 472
2014 Jun 24	2014.4772	AE-AW-E6 AW-E6-W7	15	79	HR 5329
2014 Jun 25	2014.4799	AE-AW-E6 AW-E6-W7	15	79	HR 5329
2014 Jun 26	2014.4826	AE-AW-E6 AW-E6-W7	15	79	HR 5329
2015 Mar 28	2015.2360	AC-AW-E03	10	32	HR 5329 FK5 423 FK5 622
2015 Mar 29	2015.2387	AC-AW-E03	10	32	HR 5329 FK5 423 FK5 622
2015 Apr 21	2015.3015	AC-AW-E03	10	32	HR 5329 FK5 423 FK5 622
2015 Apr 28	2015.3206	AC-AW-E03	10	32	HR 5329 FK5 622
2015 Apr 30	2015.3261	AC-AW-E03	10	32	HR 5329 FK5 423 FK5 622
2015 May 20	2015.3808	AC-AW-E03	10	32	HR 5329 FK5 677
2015 May 28	2015.4026	AC-AW-E03	10	32	HR 5329 FK5 423 FK5 677
2015 Jun 01	2015.4136	AC-AW-E03	10	32	HR 5329 FK5 423 FK5 677

Notes: Column 3 lists station names used in baselines or triangles; Cols. 4 and 5 list the minimum and maximum projected baseline lengths during the observations; and Col. 6 the calibrator stars used.

Table A.2. Astrometric results

UT Date	Julian year	Number of vis.	ρ mas	θ deg.	σ_{maj} mas	σ_{min} mas	ϕ deg.	$O - C_\rho$ mas	$O - C_\theta$ deg.
(1)	(2)	(3)	(4)	(5)	(6)	(7)	(8)	(9)	(10)
Apr 18	1989.2946	44	3.47	70.28	0.371	0.079	102.4	0.26	-0.3
Jun 19	1991.4629	59	7.22	251.89	0.208	0.098	65.3	-0.19	-0.6
Feb 28	1992.1583	39	6.98	253.18	0.198	0.075	112.3	0.23	1.8
Apr 28	1992.3226	75	8.27	254.54	0.287	0.119	84.1	0.74	0.4
May 02	1992.3336	61	7.47	256.13	0.327	0.166	83.5	0.60	0.7
Jun 08	1992.4349	87	6.39	249.32	0.222	0.062	62.6	0.26	-1.3
Mar 19	1997.2123	549	4.62	251.34	0.264	0.192	10.1	0.02	2.6
Mar 26	1997.2315	549	7.25	252.08	0.226	0.131	135.0	0.04	-0.0
May 08	1997.3492	337	3.73	247.60	0.409	0.156	121.7	-0.00	0.3
Jun 19	1997.4642	234	3.12	77.49	0.345	0.136	135.0	-0.01	4.0
Jun 21	1997.4697	316	2.08	77.18	0.414	0.183	154.8	-0.10	-1.1
Jun 22	1997.4724	450	1.47	76.79	0.345	0.136	135.0	0.02	-6.9
Jun 26	1997.4833	237	2.27	250.11	0.478	0.181	116.5	0.28	8.4
Jun 27	1997.4861	328	2.82	236.87	0.264	0.192	10.1	0.07	-8.0
Jul 04	1997.5052	656	6.26	248.55	0.226	0.131	135.0	-0.21	-2.5
Jul 08	1997.5162	246	7.42	254.26	0.453	0.117	135.0	0.01	1.8
Jul 09	1997.5189	246	7.39	252.07	0.740	0.186	122.1	-0.14	-0.7
Jul 13	1997.5299	137	7.85	257.55	0.789	0.268	135.0	0.28	3.6
Jul 14	1997.5326	410	7.32	252.20	0.414	0.183	115.2	-0.15	-2.1
Mar 05	2013.1740	420	6.25	256.07	0.226	0.131	135.0	-0.01	-0.3
Mar 06	2013.1767	360	5.62	256.83	0.292	0.143	157.7	-0.31	0.0
Mar 07	2013.1794	330	5.39	256.09	0.582	0.226	22.4	-0.18	-1.2
May 24	2013.3930	445	2.62	242.84	0.226	0.131	135.0	-0.01	-1.7
May 25	2013.3957	1208	3.43	244.31	0.264	0.192	10.1	0.09	-2.2
May 26	2013.3985	480	4.11	245.67	0.374	0.221	121.5	0.11	-2.1
May 27	2013.4012	1530	4.53	250.81	0.292	0.143	157.7	-0.07	2.1
May 30	2013.4094	1649	6.04	251.26	0.226	0.131	135.0	-0.01	0.7
May 31	2013.4122	1829	6.30	253.41	0.264	0.192	10.1	-0.12	2.4
Jun 01	2013.4149	1620	6.66	253.59	0.226	0.131	135.0	-0.07	2.2
Jun 03	2013.4204	1304	7.27	252.46	0.292	0.143	157.7	0.05	0.4
Jun 04	2013.4231	1920	7.40	253.14	0.264	0.192	10.1	0.01	0.7
Jun 05	2013.4259	1608	7.60	253.22	0.226	0.131	135.0	0.09	0.5
Jun 07	2013.4313	60	7.56	255.34	1.058	0.490	115.7	-0.07	2.0
Jun 08	2013.4341	339	7.63	257.33	0.576	0.317	143.8	0.00	3.7
Jun 10	2013.4395	450	7.63	255.59	0.264	0.192	10.1	0.14	1.4
Jun 11	2013.4423	457	7.72	256.67	0.414	0.183	154.8	0.35	2.1
Jun 13	2013.4478	171	7.15	258.39	0.385	0.243	162.3	0.13	3.2
Jun 15	2013.4532	300	6.77	258.07	0.688	0.171	161.5	0.26	2.1
Jun 16	2013.4560	300	6.38	256.03	0.345	0.136	135.0	0.17	-0.4
Jun 17	2013.4587	359	5.95	256.65	0.483	0.197	136.6	0.08	-0.2
Jun 24	2014.4772	4248	0.80	12.46	0.226	0.131	135.0	0.14	-15.8
Jun 25	2014.4799	4186	1.23	41.58	0.226	0.131	135.0	0.07	-9.7
Jun 26	2014.4827	4334	1.81	57.29	0.226	0.131	135.0	0.09	-2.6
Mar 28	2015.2356	875	5.39	247.62	0.226	0.131	135.0	-0.04	-2.2
Mar 29	2015.2383	620	5.84	246.62	0.483	0.197	133.4	-0.04	-3.7
Apr 21	2015.3013	895	4.11	256.71	0.344	0.126	135.0	0.18	-3.5
May 20	2015.3807	476	5.93	249.06	0.514	0.261	177.8	-0.18	-1.6
May 28	2015.4026	1065	7.46	249.77	0.345	0.136	135.0	-0.17	-3.6
Jun 01	2015.4135	630	7.23	251.26	0.483	0.197	136.6	-0.12	-3.3

Notes: Column 3 lists the number of visibility measurements obtained; Cols. 4 and 5 separation and position angle of the binary components (at local midnight of the date of observation); Cols. 6, 7, and 8 the major and minor axis, and the position angle of the astrometric error ellipse, respectively. Columns 9 and 10 list the offsets in separation and angle between the measurements and the predicted orbit positions.

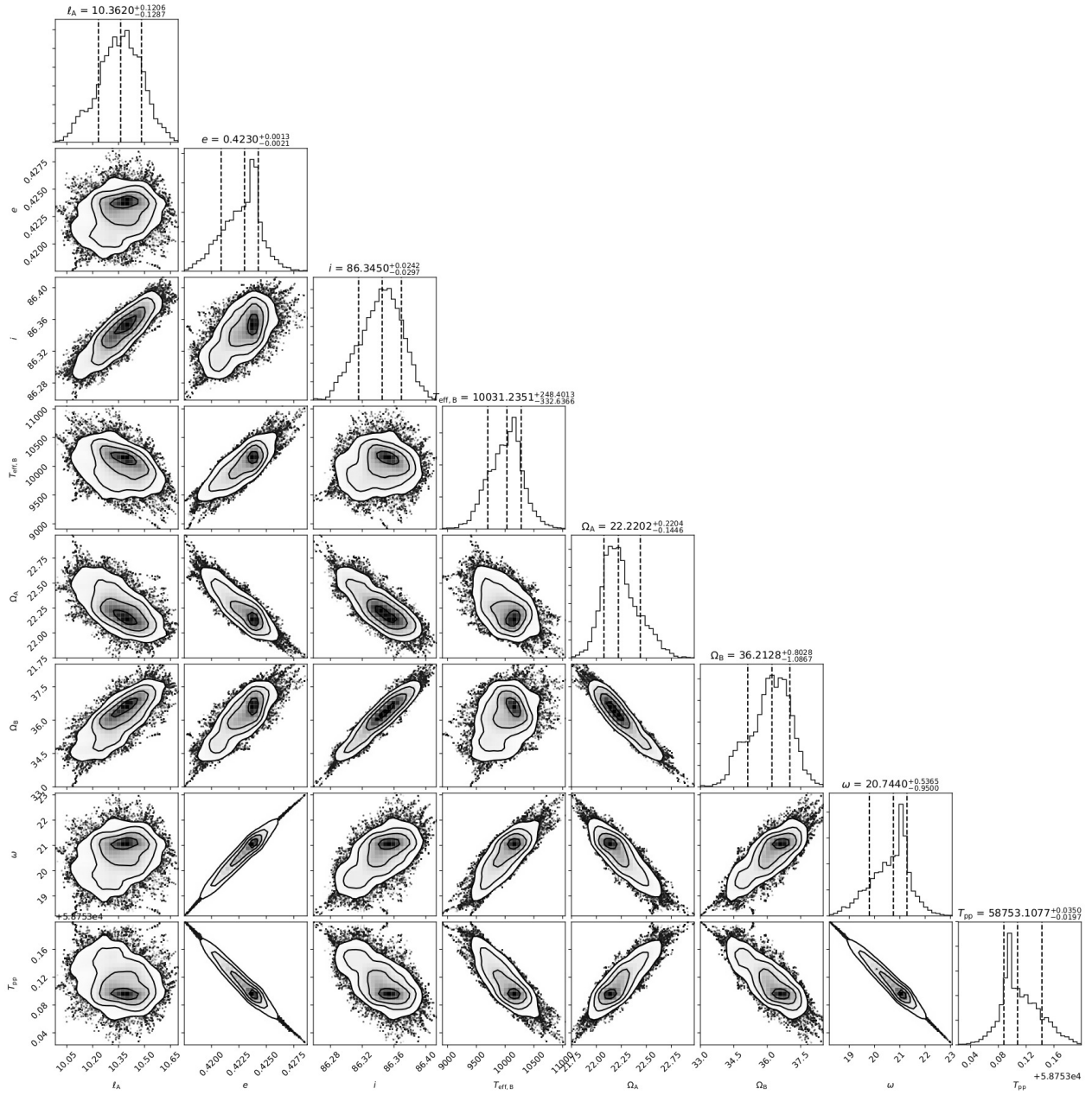## Appendix B: EMCEE calculations of the uncertainties in the light curve analysis

Fig. B.1. MCMC determination of the light curve parameters and accompanying uncertainties for TESS observations of α Dra in Part 1 (Sectors 14, 15, and 16). A strong correlation between parameters is present, as expected for partial (almost grazing) eclipses. The posterior distribution densities are plotted (solid contours). The histogram distributions (solid lines) are plotted across the associated quantity with 16th, 50th, and 84th percentiles levels (dashed lines).
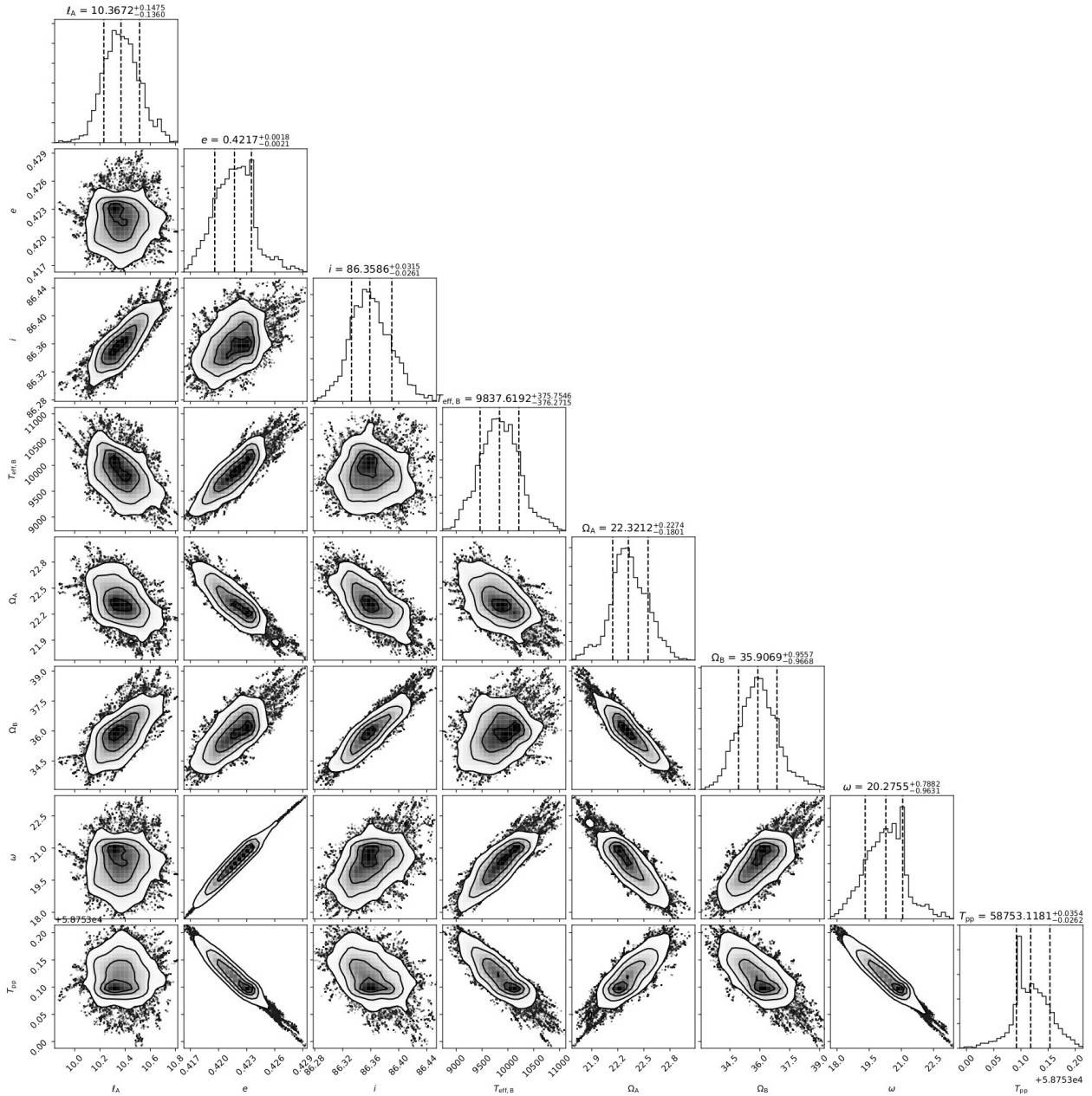
Fig. B.2. Same as Fig. B.1, but for TESS observations of α Dra in Part 2 (Sectors 21 and 22).